Structures Research
Report 2012/ 94753

University of Florida
Civil and Coastal Engineering

UF

GATOR
Engineering
University of Florida
Civil and Coastal Engineering

Final Report June 2012

Development of multi-barge flotilla finite element models for use in probabilistic barge impact analysis of flexible walls

Principal investigator:
Gary R. Consolazio, Ph.D.

Graduate research assistant:
Robert A. Walters

Department of Civil and Coastal Engineering
University of Florida
P.O. Box 116580
Gainesville, Florida 32611

Sponsor:
Digital Engineering and Imaging, Inc.
U.S. Department of the Army
Point of Contact:
Robert C. Patev, Senior Risk Advisor, Risk Management Center, US Army Corps of Engineers

Contract:
UF Project No. 94753

DISCLAIMER

The opinions, findings, and conclusions expressed in this publication are those of the authors and not necessarily those of the U.S. Army Corps of Engineers or Digital Engineering and Imaging, Inc.

ACKNOWLEDGEMENTS

The authors would like to thank the U.S. Army Corps of Engineers and Digital Engineering and Imaging, Inc. for providing the funding that made this research possible.

EXECUTIVE SUMMARY

Current design practices for waterway guidance and protection structures employed by the U.S. Army Corps of Engineers are based on data developed from full-scale impact experiments conducted on rigid guidance structures. Given that the inventory of navigational structures designed by the USACE also includes flexible systems, it is important to determine whether application of the current impact load determination procedures to such structures produces appropriate, overly conservative, or unconservative designs. This study addresses this issue by developing, verifying, and validating a flexible guide wall finite element model that accounts for nonlinear concrete and mild reinforcing steel behavior, the effects of post-tensioned segmental concrete construction, and a variable cross-sectional shape. Subsequently, impact simulations are conducted with the wall model and a high-resolution nonlinear multi-barge flotilla model at various impact angles and impact velocities to quantify flotilla impact forces on the wall. Results reveal that peak impact forces are primarily a function of mass contained within the first row of barges in the flotilla. Because cable lashings are relatively flexible in comparison to the stiffnesses of individual barges, during a flotilla-wall collision event, only barges in the first row of the flotilla are redirected immediately by the wall. Consequently, flotilla width is found to strongly influence peak impact force while barge flotilla length is found to have minimal, almost negligible, influence. These results also suggest that the common design practice of using only flotilla momentum, which depends on both the width and length of a flotilla, to predict peak impact force is not likely to lead to the most efficient design standards when applied to multi-barge flotilla impacts.

TABLE OF CONTENTS

CHAPTER 1
INTRODUCTION

1.1 Introduction

Navigational guidance structures serve an important role in helping to ensure safe operations at locks and dams throughout the United States. These structures provide dual functionality by aiding vessel operators in aligning their vessels with locks, and by protecting nearby waterway facilities such as hydroelectric dams. With the high volume of lockages that occur on the navigable waterways of the United States, guidance structures can be subjected to daily impacts from vessels; most commonly barge flotillas. Procedures currently employed by the U.S. Army Corps of Engineers (USACE) for the calculation of barge impact forces on waterway guidance and protection structures are based primarily on data obtained from investigations of barge impacts on *rigid* structural systems. However, given that the inventory of navigational structures designed by the USACE also includes *flexible* systems, it is important to determine whether application of the current impact load determination procedures to such structures produces appropriate, overly conservative, or unconservative designs.

Typical approaches used to quantify impact loads involve relatively expensive impact experiments, which are often limited—for safety reasons—to low-energy impact conditions. However, with ever increasing ability to generate and analyze complex finite element models, impact forces imparted on structures by barge flotillas can be quantified using finite element analysis with accuracy suitable for design. Furthermore, finite element simulation provides the ability to quantify impact forces for high-energy impact events that push materials well into their nonlinear ranges. Coupled together with experimental validation data, finite element impact simulation can provide significant advantage in the development of accurate and efficient design guidelines for the USACE.

1.2 Objective

The work described in this report documents the development of a flexible guide wall finite element (FE) model and dynamic FE impact simulations conducted on the guide wall. A high-resolution, nonlinear FE barge flotilla model has been used as the impacting vessel for the simulations in this study. Impact forces have been quantified for a variety of impact conditions by varying angle of obliquity and impact velocity. Force time-history results from these simulations have been compared to those from the Winfield Lock and Dam experiments (Barker et al. in press). In addition, the influence of a load-measurement beam that was attached to the corner of the test barges in both the Robert C. Byrd Lock and Dam experiments (Patev et al. 2003) and the Winfield Lock and Dam experiments, has been investigated to determine the effect this system has on measured impact force.

1.3 Scope

In this study, high-resolution barge flotilla FE models, comprised of either nine (9) or fifteen (15) individual jumbo hopper river barge FE models, are simulated impacting a flexible guidance structure FE model to quantify impact forces and guide wall deflections. The flexible guidance structure is modeled after an existing guide wall at the Winfield Lock and Dam. Impact conditions focus on glancing impacts (angles ≤ 30°) and impact velocities ranging from two (2) feet per second (fps) to five (5) fps. The study objectives are achieved by completing the following tasks:

- Develop a deformable, materially-nonlinear FE model of the guide wall at the Winfield Lock and Dam
- Develop FE models of the foundation (cell and thrust block) and of the connections between the guide wall and foundation
- Develop a FE model of the load-measurement beam used at the Winfield Lock and Dam and Robert C. Byrd Lock and Dam experiments
- Investigate the influence of the load-measurement beam, and verify behavior of the flexible wall, by conducting dynamic FE impact simulations of impact conditions similar to those used at the Winfield Lock and Dam
- Conduct dynamic FE impact simulations to quantify impact forces and deflections over a range of typical impact angles and initial velocities

CHAPTER 2
BARGE FLOTILLA FINITE ELEMENT MODEL

2.1 Flotilla finite element model overview

Each impact simulation conducted for this study utilized a high-resolution finite element model of a barge flotilla. A barge flotilla, such as the one shown in Figure 2.1, is an assembly of individual barges, typically of similar size and configuration, which are connected together by a series of wire ropes (also known as lashings). For this study, two specific barge flotilla configurations are modeled: a 3x5 barge flotilla (consisting of three strings, or columns, of five barges per string – 15 barges total) and a 3x3 barge flotilla (consisting of three strings of three barges per string – 9 barges total).

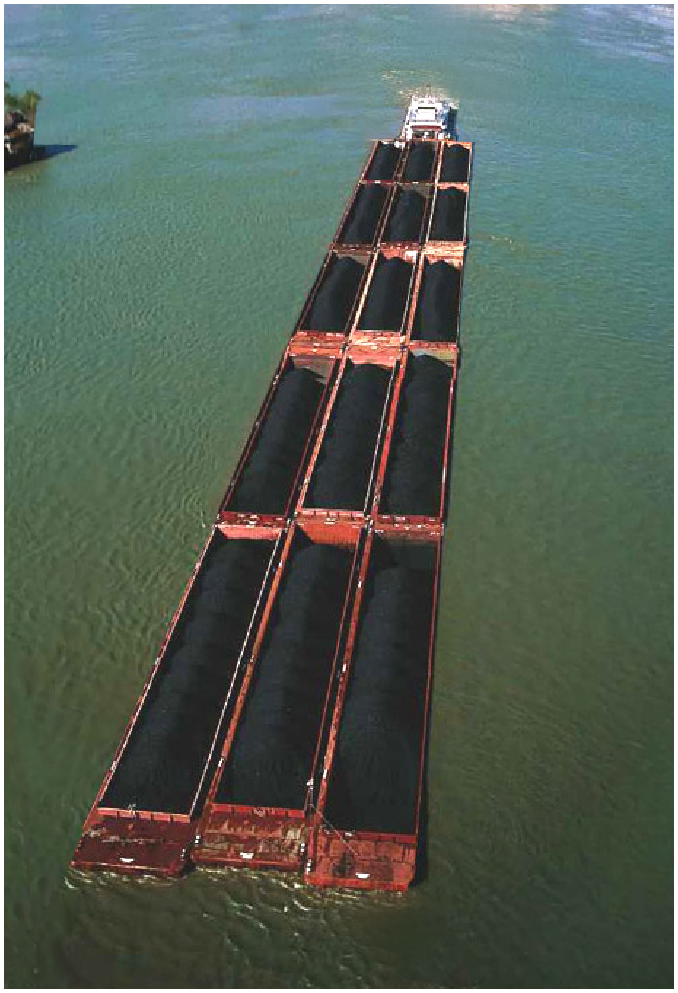

Figure 2.1. Typical 3x5 barge flotilla in transit (after USACE 2007)

The barge flotilla FE models used in this study are created using the same methodology as that documented in the report *Development of Finite Element Models for Studying Multi-barge Flotilla Impacts*" (Consolazio et al. 2010). Nevertheless, a brief overview of the barge flotilla FE model is described in the present report to provide self-contained documentation of the capabilities of the model.

Each barge flotilla FE model is comprised of a series of jumbo hopper river barges measuring 195 ft long by 35 ft wide and weighing 2000 tons each (where 1 ton = 2000 lbs). Two configurations of this jumbo hopper river barge are employed in each flotilla model: single-raked and double-raked. Single-raked barges are raked (tapered through the depth) at the bow only, whereas double-raked barges are raked at both the bow and stern. Single-raked barges are present at the fore-most and aft-most barge positions of each string of barges while double-raked barges are only present in between the fore- and aft-most barges in each string. A schematic of each jumbo hopper barge is shown in Figure 2.2.

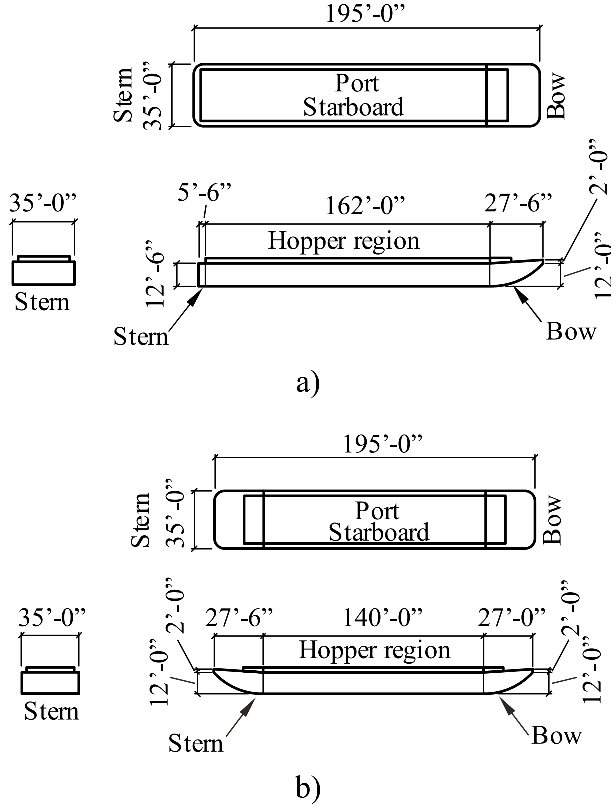

Figure 2.2. Jumbo hopper barge schematics:
a) Single-raked barge; b) Double-raked barge

The two barge flotilla configurations used in this study are shown in Figure 2.3. The 3x5 barge flotilla has overall dimensions of 975 ft by 105 ft (length by width) with a total weight of 30,000 tons and the 3x3 barge flotilla has overall dimensions of 585 ft by 105 ft (length by width) with a total weight of 18,000 tons. A rendering of the FE model of each flotilla is shown in Figure 2.4.

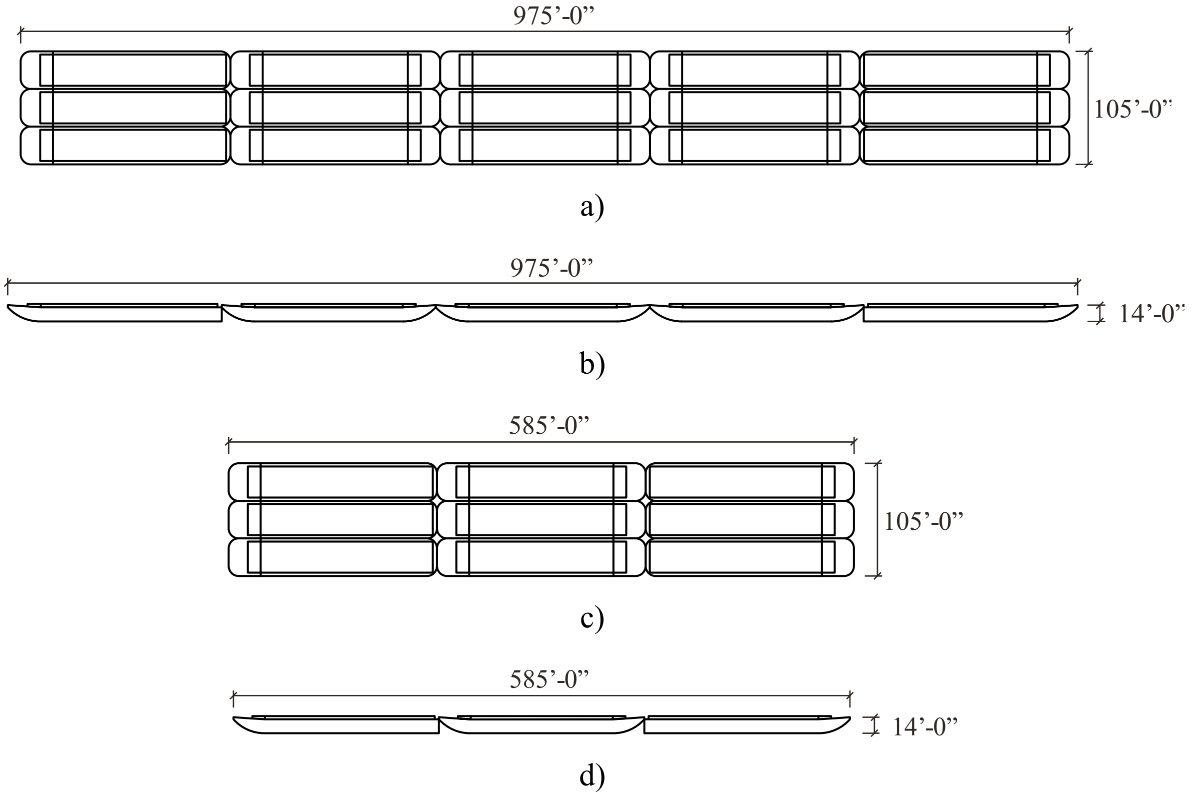

Figure 2.3. Jumbo hopper barge flotilla schematics:
a) 3x5 plan view; b) 3x5 elevation view; c) 3x3 plan view; d) 3x3 elevation view

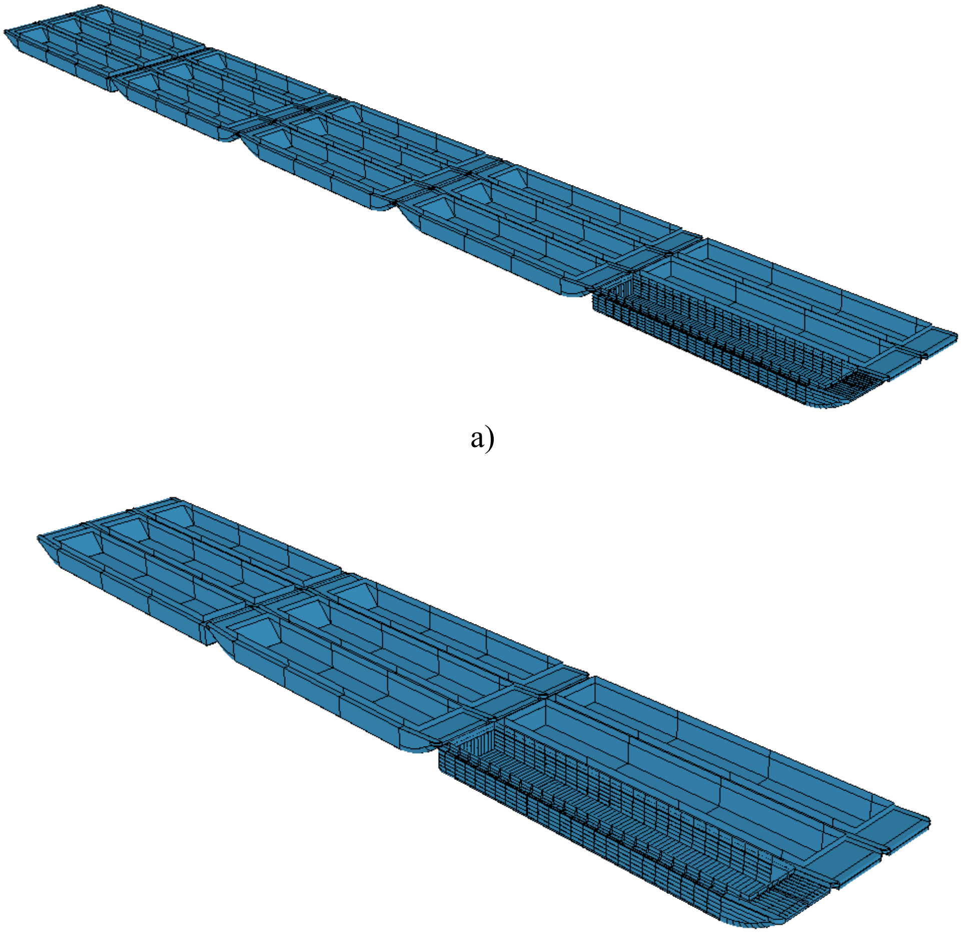

a)

b)

Figure 2.4. Jumbo hopper barge flotilla FE model (mesh not shown for clarity):
a) 3x5 flotilla; b) 3x3 flotilla

2.2 Structural modeling

Two types of individual barge FE models are used within the flotilla models for this study. A single highly discretized barge within each flotilla, referred to as the *impacting* barge, is the only barge to make physical contact with the target structure (structure to be impacted). The high level of discretization associated with the impacting barge is necessary to enable accurate representation of the contact interaction between the target structure and impacting barge. The remaining barges within a given flotilla are referred to as *non-impacting* barges. The primary role of non-impacting barges is to facilitate modeling of both the dynamic response resulting from barge-to-barge contact and the lashing interactions of adjacent barges during impact. Note that non-impacting barges never make contact with the target structure.

2.2.1 Impacting barge

The high-resolution impacting barge FE model is composed of more than 900,000 nonlinear shell elements modeled in LS-DYNA (LSTC 2009); is consistent with available detailed structural plans; and is made up of three barge zones: the bow zone, the stern zone, and the hopper zone. Each zone is discretely modeled with internal structural members and external plate surfaces. Internal structural members consist of angle, channel, or plate sections. Internal member thicknesses and external plate thicknesses vary between 5/16 in. and 5/8 in., as determined by the structural plans. Figure 2.5 shows a rendering of the impacting barge. An example of the high level of mesh discretization is demonstrated in Figure 2.6, which shows a rendering of the bow zone of the impacting barge FE model.

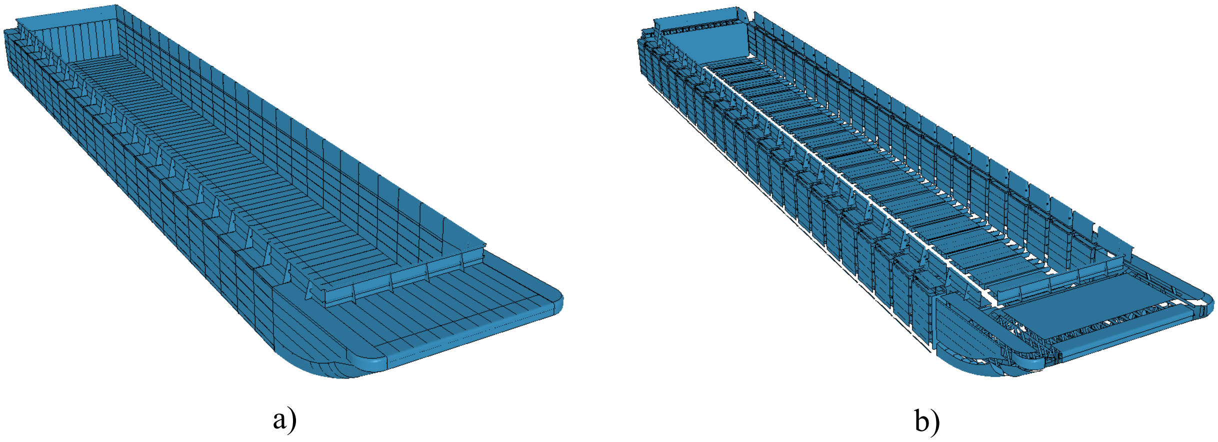
a) b)

Figure 2.5. Jumbo hopper barge finite element model (mesh not shown for clarity):
a) Perspective view; b) Exploded view

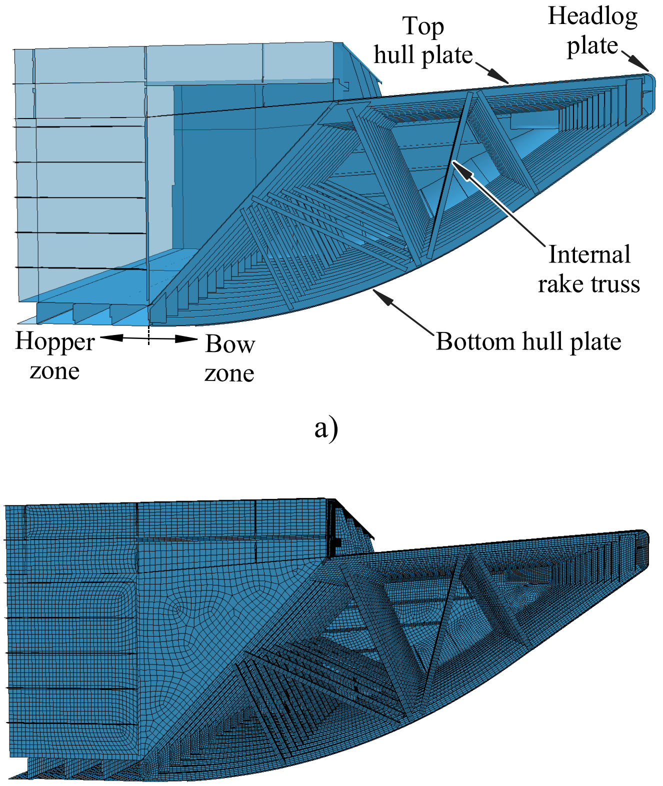

a)

b)

Figure 2.6. Barge bow zone: a) Structural configuration; b) Finite element mesh

The impacting barge is given a nonlinear constitutive relationship (effective true stress vs. effective plastic strain) representing A36 structural steel, which is shown in Figure 2.7. This relationship is employed for all structural and plate members within the barge FE model, which are meshed using 4-node fully integrated shell elements. Importantly, each structural member is modeled with sufficient mesh density to allow for local buckling and local material failure. Material failure is represented by element deletion within LS-DYNA and occurs when the effective plastic strain of the steel reaches 0.2 in./in.

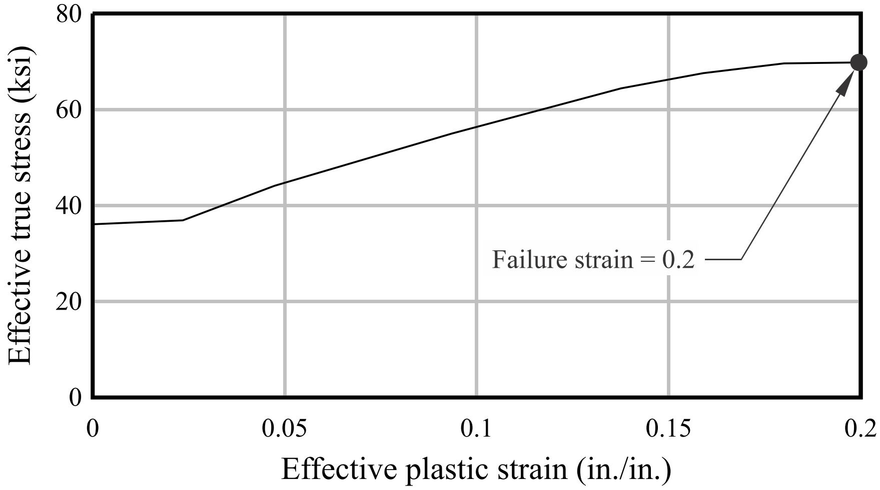

Figure 2.7. Barge structural steel stress-strain relationship

In addition to the base constitutive relationship, a model to account for strain rate effects is also included. Strain rate effects occur at the material level and act to increase the overall effective stiffness of structural members by raising the yield stress of the material as the plastic strain rate increases. In this study, these effects are modeled using the Cowper-Symonds strain rate model, which is given by:

$$\frac{\sigma^y_{dynamic}}{\sigma^y_{static}} = \left[1 + \left(\frac{\dot{\varepsilon}^p_{eff}}{C}\right)^{1/Q}\right] \tag{1}$$

In this relationship, dynamic yield stress ($\sigma^y_{dynamic}$) is obtained by modifying the static yield stress (σ^y_{static}) based on the effective plastic strain rate ($\dot{\varepsilon}^p_{eff}$) and two material-dependent parameters, C and Q. For mild steel, C and Q are taken as 40.5 sec^{-1} and 5, respectively (Jones 1997). In Figure 2.8, the increase of dynamic yield stress (relative to the static yield stress) predicted by the Cowper-Symonds model is illustrated for mild steel.

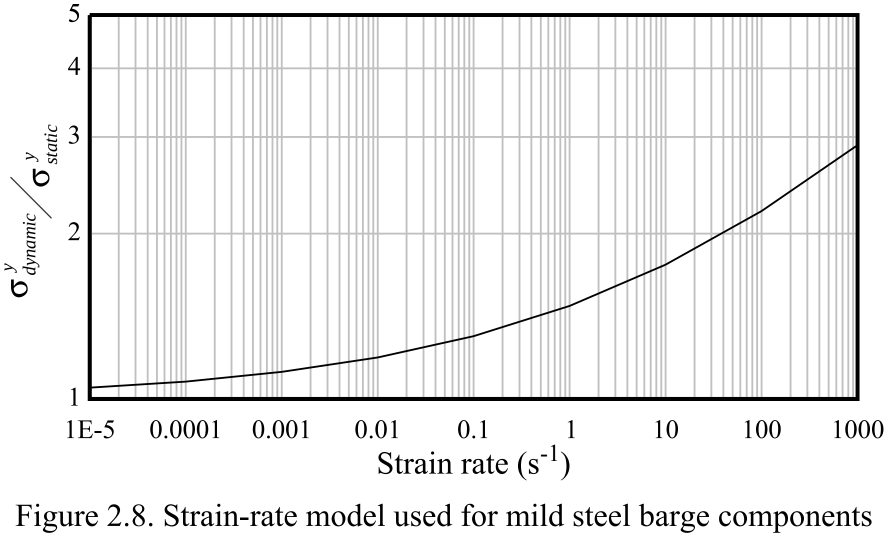

Figure 2.8. Strain-rate model used for mild steel barge components

2.2.2 Non-impacting barge

The primary role of the non-impacting barge FE model is to provide a means of efficiently representing the mass-related inertial properties of a barge as well as the dynamic interactions between barges (through contact and lashings) during and after impact. In practical terms, it is not computationally feasible to utilize a high-resolution deformable barge model at each position within a flotilla to model these effects. For this reason, the non-impacting barge is modeled in a way that retains the external geometry of a high-resolution barge, as well as the inertial and mass properties, but has a lower mesh resolution than the high-resolution barge FE model. The low-resolution non-impacting barge has approximately 4,000 shell elements compared to the 900,000 shell elements of the high-resolution impacting barge.

Shell elements defining the external geometry of the non-impacting barge are modeled as rigid elements, and no internal structural elements are modeled. Inertial and mass properties measured using the high-resolution barge model are assigned to (imposed upon) the rigid non-impacting barge. This procedure allows the non-impacting barge to mimic the rigid body dynamics of a high-resolution barge model when external forces are imposed upon it. However, being a rigid model, the appropriate structural stiffness of the non-impacting barge model, which affects barge-to-barge contact forces, is not automatically generated by the mesh. Instead, the structural stiffness of the high-resolution barge is introduced into the low-resolution non-impacting rigid barge model through contact definitions (discussed later) in a way that produces the appropriate stiffness relationship. A rendering of the non-impacting barge FE model is shown in Figure 2.9.

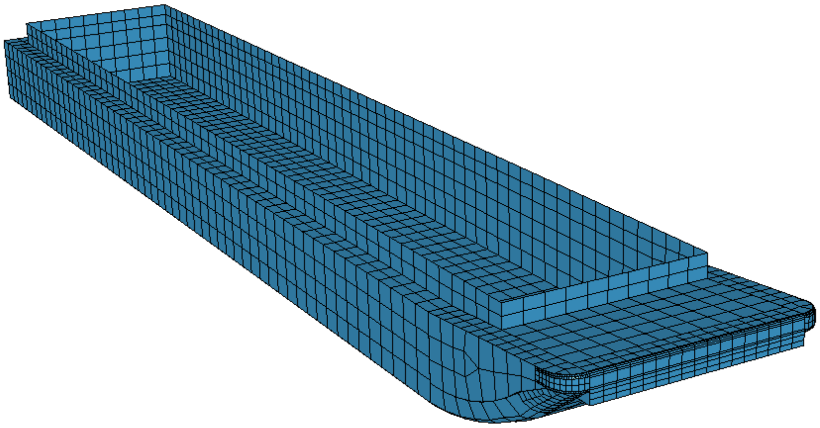

Figure 2.9. Non-impacting barge FE model (mesh shown)

2.3 Barge interactions within flotilla model

Individual barges within a barge flotilla are joined together using wire ropes (also referred to as lashings) that wrap around bitts (cylindrical posts) which are affixed to the barge deck. A photograph of a typical lashing configuration is provided in Figure 2.10. Lashing configurations used within this study are consistent with those used in the full-scale barge impact tests conducted by the USACE at Gallipolis Locks (Patev et al. 2003). Each wire rope within the FE model is assigned an appropriate geometric configuration; a set of material properties that represent the nonlinear stiffness of the lashing; and a failure criterion based on ultimate capacity. Depending upon the location of the wire rope within the overall flotilla, an appropriate ultimate tensile of either 90 kips (for 1 in. diameter wire rope) or 120 kips (for 1.25 in. diameter wire rope) is assigned. By including a failure criterion, the flotilla model has the ability to experience either full or partial break-up wherein the individual barges are free to separate from one another and move independently.

Figure 2.10. Lashing configuration on barge flotilla

Each pair of adjacent barges within a flotilla is lashed together by wrapping the barge bitts in a specific pattern, referred to as a lashing configuration. Different configurations are used to lash different types of barge pairs (end-to-end, side-to-side, or diagonal) and to resist different loads imposed by common flotilla maneuvers. Lashings are layered on top of each other when more than one configuration is required at the same location. In total, seven lashing configurations are used in the 3x3 and 3x5 barge flotilla models.

Fore/aft wires (Figure 2.11–2.12) are used to secure end-to-end barge pairs together at shared corners, providing longitudinal rigidity to each barge string. The configuration used along the exterior edges of the flotilla (L1) is unique in that it employs a 1 in. diameter wire rope rated at a 90 kip break strength. Every other configuration in the flotilla, including the fore/aft wires along the interior edges (L2–L3), uses a 1.25 in. diameter wire rope rated at a 120 kip break strength.

Breast wires (Figure 2.13) are used to connect side-to-side barge pairs together at shared corners, and act to keep the port and starboard strings from lagging behind the center string during travel. Because of their different orientations, they are sometimes referred to separately as towing wires (L4) that are engaged when the center string is pushed forward, and backing wires (L5) that are engaged when the center string is pulled backward.

Scissor wires (L6–L7, Figure 2.14) connect diagonal barge pairs together at every four-corner interface. They serve to increase flexural rigidity, allowing the flotilla to be steered more easily by the rear tug. Figure 2.15 shows each lashing configuration combination for a 3x3 barge flotilla.

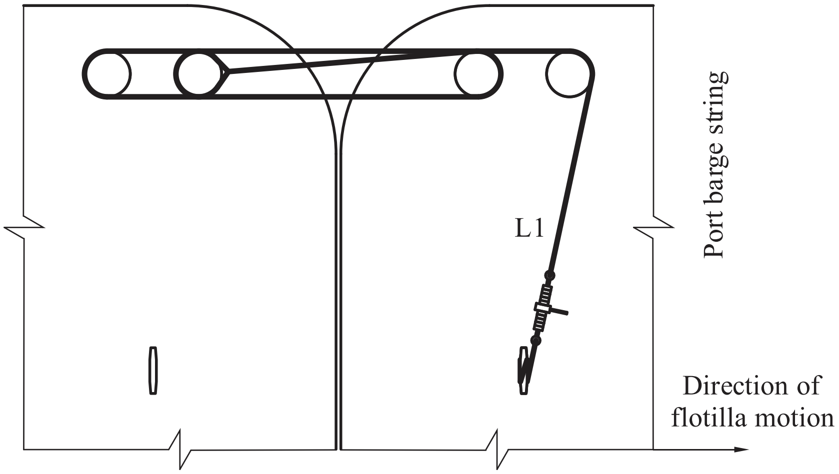

Figure 2.11. Exterior fore/aft wires (rated for 90 kip break strength)

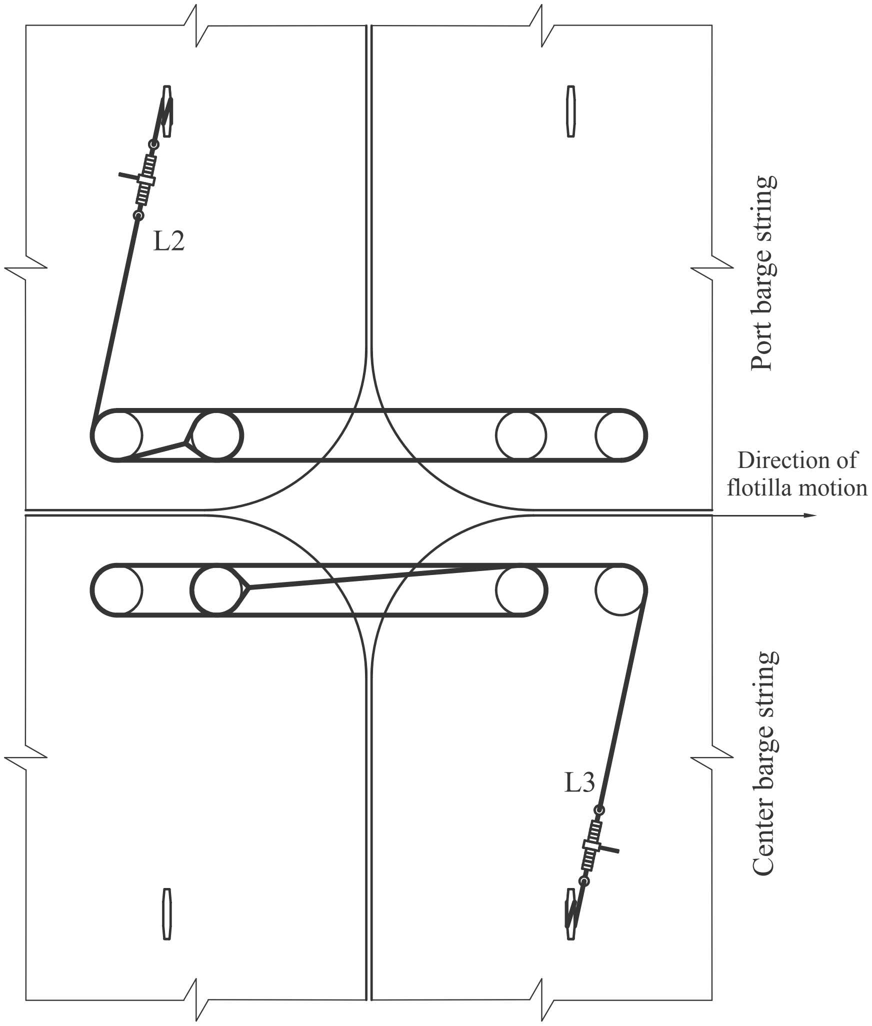

Figure 2.12. Interior fore/aft wires (rated for 120 kip break strength)

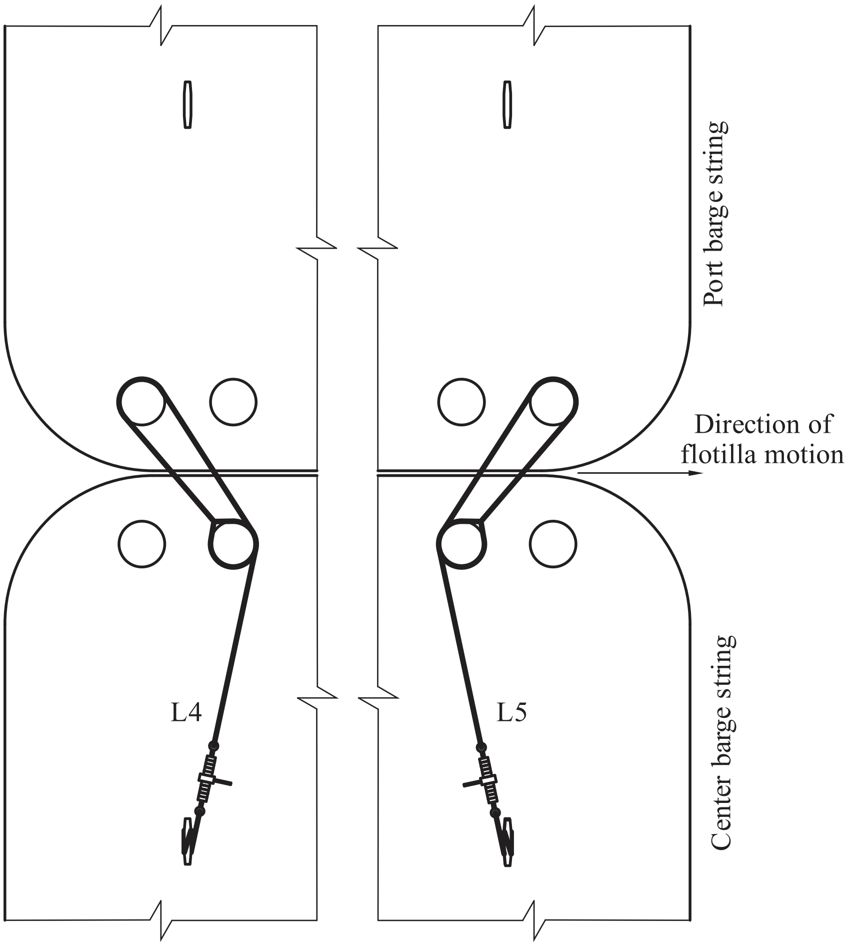

Figure 2.13. Breast wires (rated for 120 kip break strength)

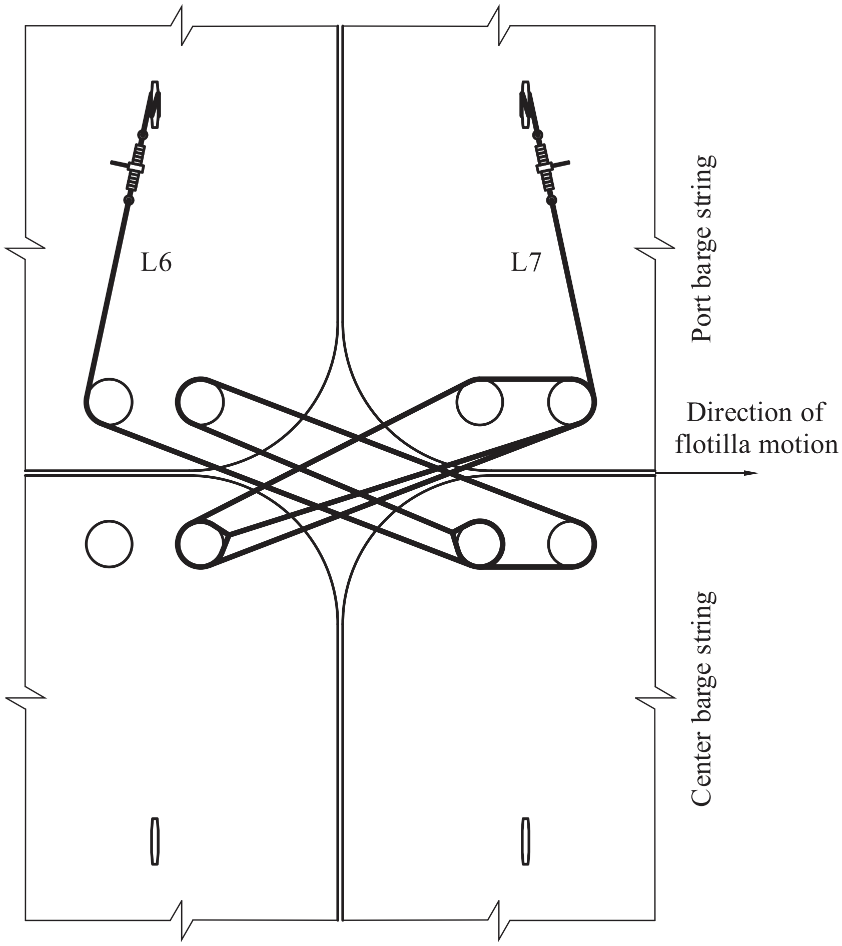

Figure 2.14. Scissor wires (rated for 120 kip break strength)

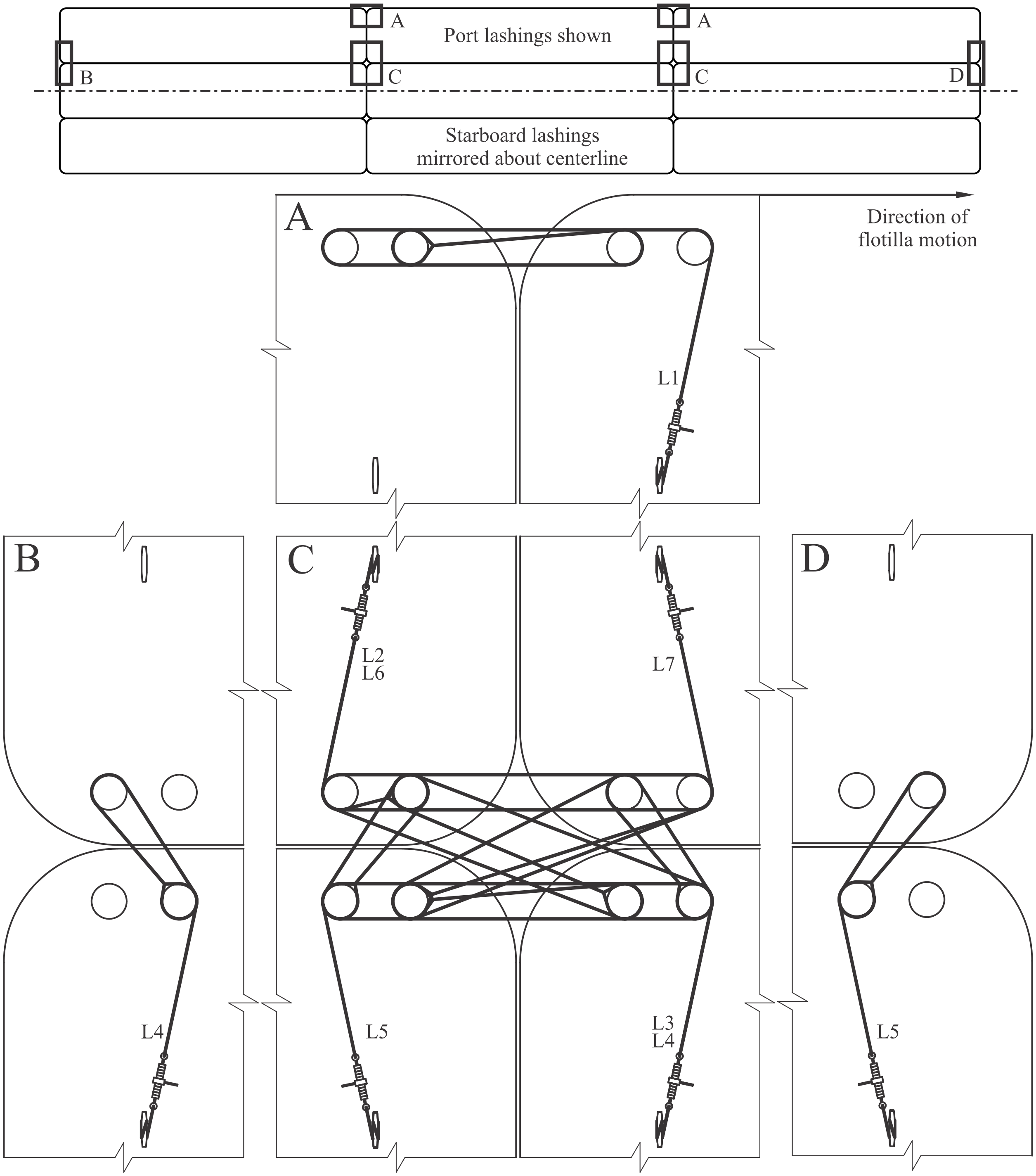

Figure 2.15. Lashing configuration combinations on a 3x3 flotilla

In addition to barges interacting with one another through lashing forces, they also interact by generating contact forces. In the barge flotilla FE model, contact definitions are defined between each set of adjacent barges. For the purposes of numerical efficiency, barges not initially in contact with each other do not have contact pairings defined between them. For instance, for a 3x3 flotilla, a barge in the lead (fore) row has no contact defined between itself and a barge in the trailing (aft) row since they are not initially adjacent to each other.

Since all barges except the impacting barge are rigidized, the contact stiffness cannot be obtained directly from the structural stiffness of the barges themselves (since the non-impacting barges are structurally rigid). Contact stiffness (and therefore structural stiffness) for a non-impacting barge is thus accounted for through the use of a prescribed contact stiffness relationship, which is representative of the stiffness of impacting barges. To obtain such relationships, high-resolution FE models of deformable barges are quasi-statically crushed together. Nonlinear force-deformation relationships (stiffnesses) can then be extracted from the results of the crushing simulation.

An example of this procedure for a bow-to-stern contact interface is shown in Figure 2.16. The force-deformation relationship obtained from this simulation (plotted in Figure 2.17) is prescribed for each bow-to-stern contact interface defined within the flotilla FE model. During an impact, as the rigid barges contact each other, the contact-impact algorithm in LS-DYNA will compute the contact penalty forces from this prescribed relationship, thereby mimicking the stiffnesses of two high-resolution deformable barges.

For each barge within the flotilla, three types of contact may be defined: side-to-side contact; bow-to-bow contact; and bow-to-stern contact. For each such case, a force-deformation relationship is generated from a high-resolution crushing simulation, and then applied to the appropriate contact definitions within the flotilla FE model.

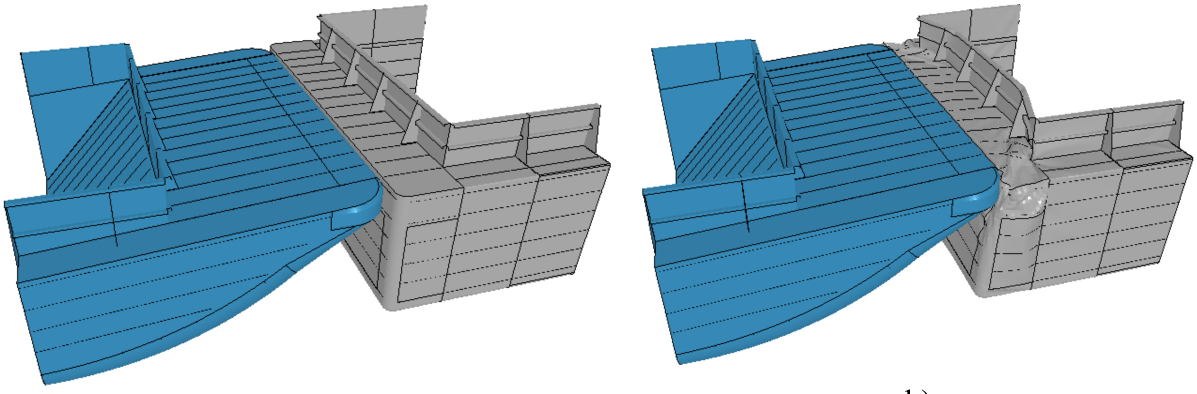
a)

b)

Figure 2.16. Bow-to-stern FE crushing simulation for determining contact stiffness of rigid barges: a) At beginning of simulation; b) During simulation

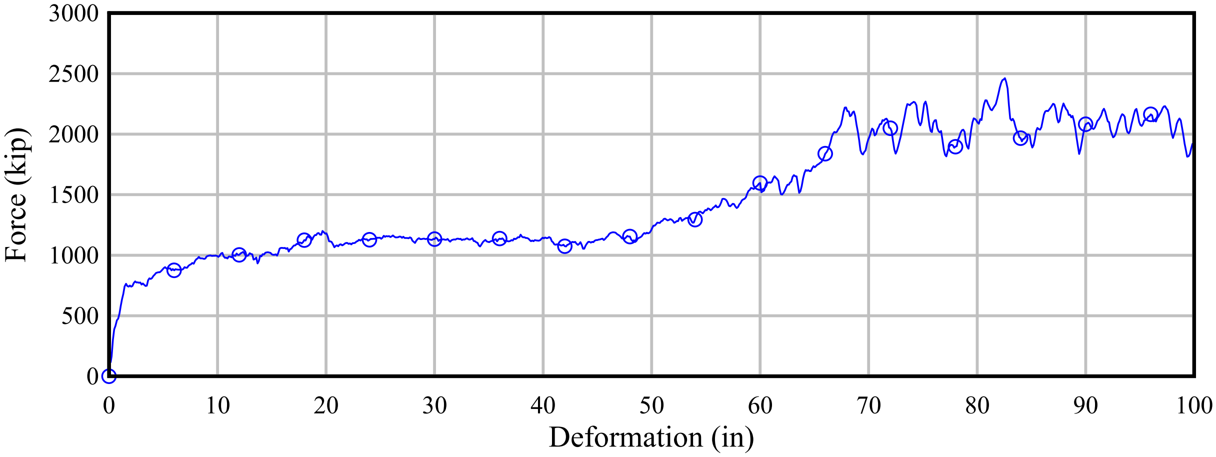

Figure 2.17. Force-deformation relationship for bow-to-stern contact stiffness of rigid, non-impacting barges

2.4 Additional modeling considerations

In each impact simulation conducted in this study, the effects of both gravitational forces and buoyancy forces acting on the barge flotilla are included. Buoyant uplift forces underneath each barge are modeled by introducing individual buoyancy springs over the bottom surface of the barge model. For the high-resolution barge model, approximately 26,400 discrete springs are attached to the barge bottom nodes, whereas each non-impacting barge employs approximately 900 buoyancy springs.

The stiffness of each buoyancy spring is computed by determining the tributary area of the barge bottom surface supported by the spring, and then multiplying this value by the density of water (62.4 lb/ft^3). By using a large number of springs with relatively small tributary areas, the resulting stiffness values are small, ranging from 0.001 kip/in to 0.004 kip/in, thereby precluding the development of unrealistically concentrated buoyant forces during barge motions.

Each buoyancy spring is 200 in. in length and connects to a support node (above the barge) that is freely able to translate in the horizontal plane (Figure 2.18) but restrained against vertical motion. As such, the barge model “hangs” from the collection of buoyancy springs and is able to translate arbitrarily large distances in the horizontal plane (plan view) without resistance. Vertical motions of the barge, however, cause appropriate changes in the distribution of vertical uplift forces, which are based on changes in the submerged depth of the barge. Because the buoyancy springs are always in tension, the vertical support node of each spring “tracks” (in plan view) with the corresponding node at the bottom surface of the barge. Consequently, the buoyancy springs remain vertical at all points during the simulation, regardless of the horizontal motions that the flotilla may undergo. This is particularly beneficial should a partial or full flotilla breakup occur during a simulation. Additional aspects of buoyancy modeling, such as calibration of the buoyancy springs and gapping of buoyant springs at the raked barge bow, are described in Consolazio et al. (2010).

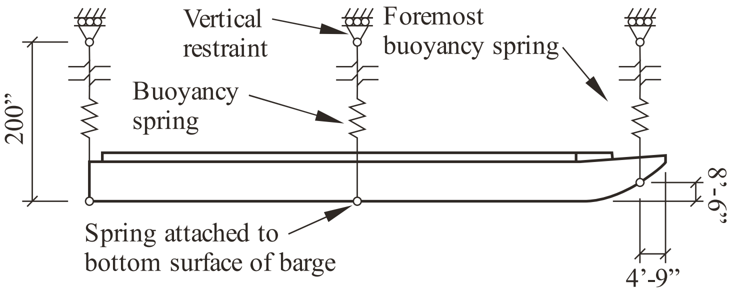

Figure 2.18. Barge buoyancy spring schematic

CHAPTER 3
FINITE ELEMENT MODELING OF FLEXIBLE GUIDANCE STRUCTURE

3.1 Introduction

In this study, a portion of the lock approach wall at the Winfield Lock and Dam (Figure 3.1) in Red House, WV is modeled with finite elements to conduct barge flotilla impact simulations. The lock approach wall is a segmental post-tensioned concrete wall (referred to as a flexible wall) that is simply supported by a foundation at each end. Each foundation is comprised of a concrete cell and concrete thrust block, which connect to the flexible wall using bearing pads and tieback anchors.

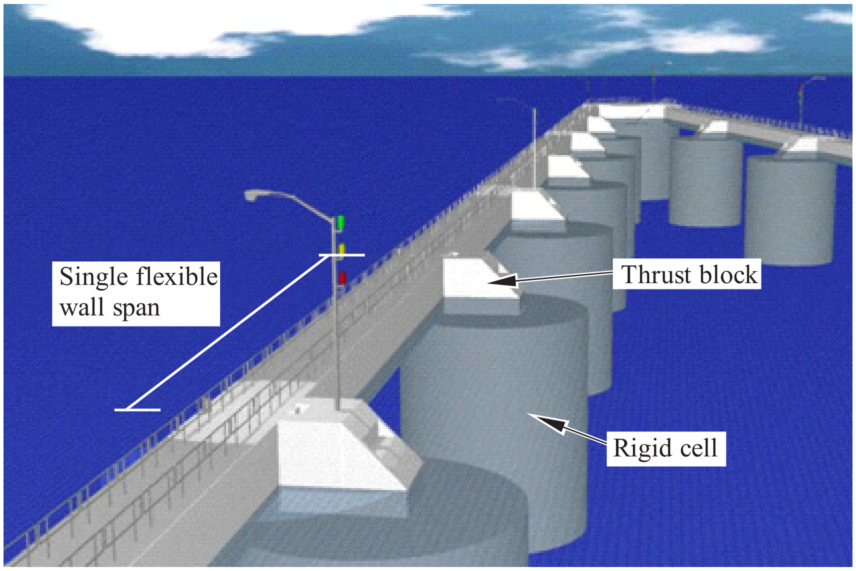

Figure 3.1. Rendering of flexible wall guidance system
(After source: Stingray Surf Graphics, Inc.)

The specific portion of the Winfield Lock and Dam considered in this study consists of a single span flexible wall unit and two foundation structures. The flexible wall is modeled using a combination of solid, shell, and beam elements that represent the concrete cross section and internal reinforcement. Foundation structures are modeled with solid elements, and bearing pads and tieback anchors are modeled with beam elements. Nonlinear materials are utilized where necessary to ensure accurate representation of the flexible wall response during impact. A rendering of the FE model of the flexible wall and support system is provided in Figure 3.2.

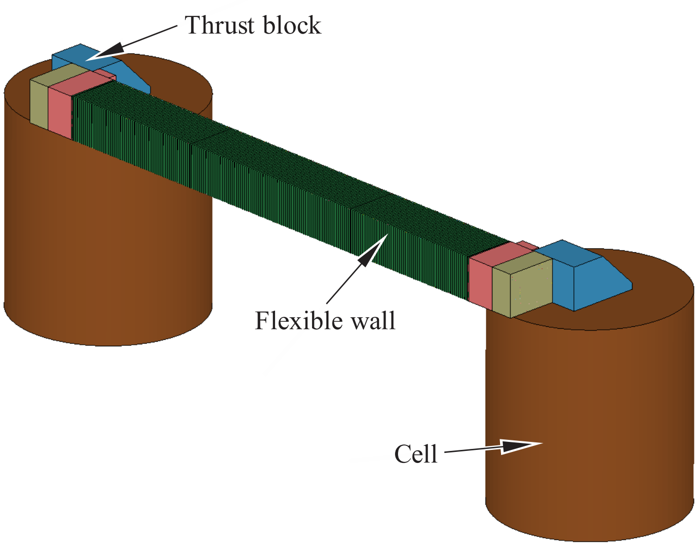

Figure 3.2. Flexible wall finite element model

3.2 Development of rigid cell and thrust block finite element models

Each flexible wall span is supported by two foundation assemblies that consist of a concrete cell footing and a concrete thrust block. A schematic of the concrete cell and concrete thrust block is shown in Figure 3.3. Each cell is a massive cylindrical reinforced concrete structure with a diameter of 35 ft 6 in. and a height of 39 ft 2 in, approximating the depth to the top of rock in the channel. Cast integrally with each cell is a thrust block, also made of reinforced concrete, that measures approximately 10 ft by 14 ft with a height of 8 ft. Each thrust block and rigid cell connect to the flexible wall span using a series of bearing pads and tieback anchors as shown in Figure 3.4.

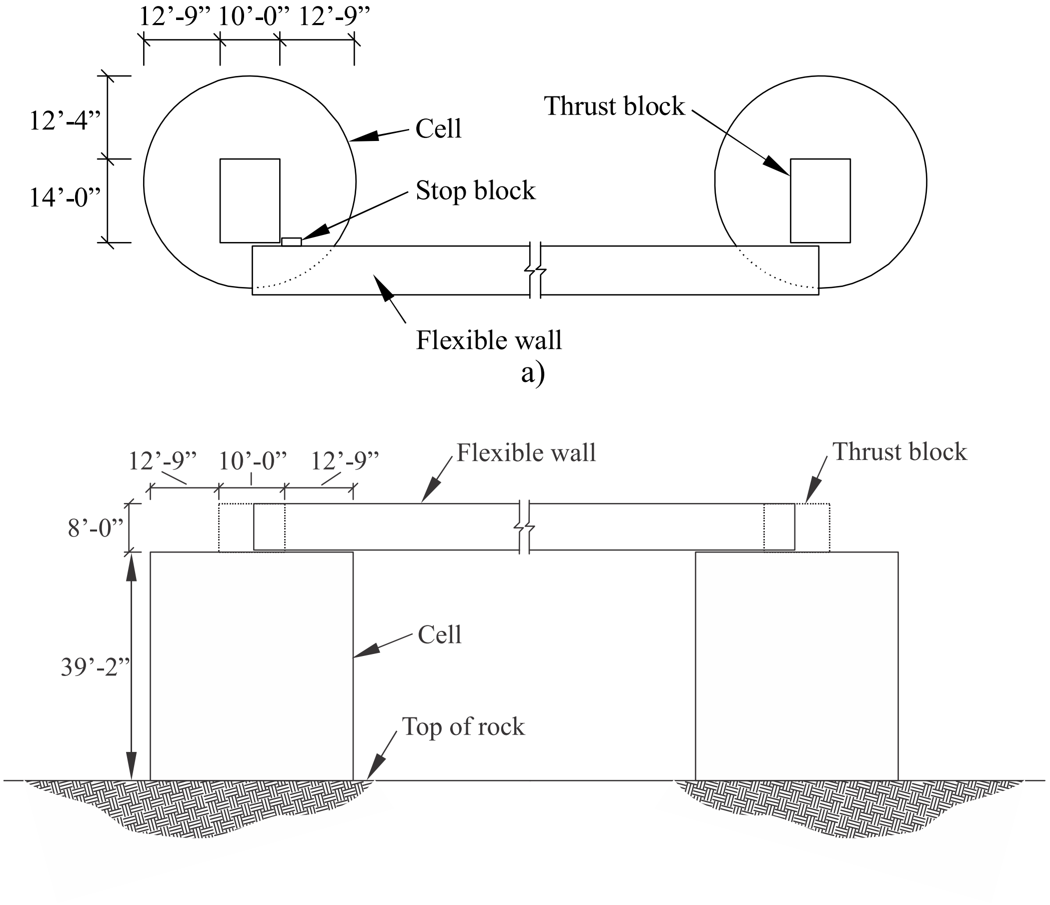

a)

b)

Figure 3.3. Schematic of foundations and flexible wall:
a) Plan view; b) Elevation view

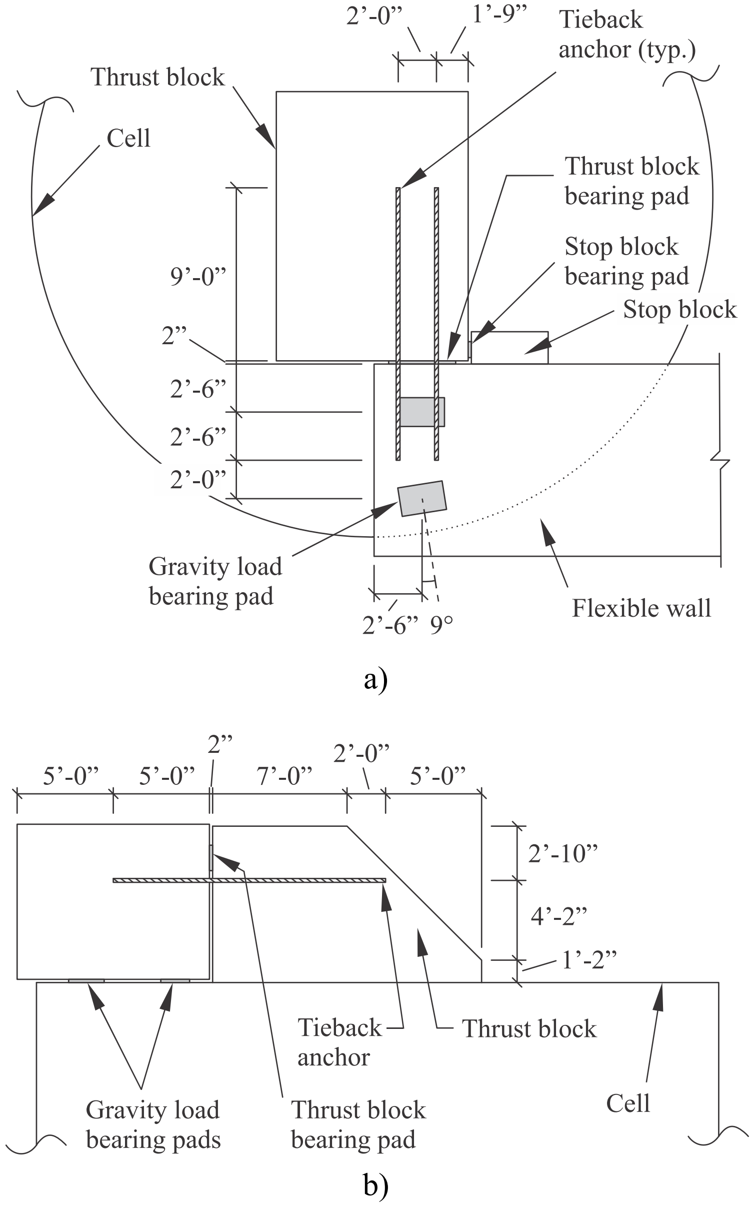

Figure 3.4. Schematic of foundation assemblies with connection details: a) Plan view; b) Section view

Since the concrete cell is considerably stiffer and more massive than the flexible wall, the deformations of the cell footing during impact will have a negligible contribution to the response of the overall system. For this reason, the concrete cell is modeled as rigid, and is therefore referred to as a rigid cell. Each rigid cell is modeled with solid elements (Figure 3.5a) having a rigid material model and a unit weight of 150 $\mathrm{lb/ft^3}$ to be representative of concrete. Because each cell is rigid, soil properties are not considered and therefore a fixed boundary condition is applied to bottom of each cell. The assumption of negligible soil response and rigid cell displacement is based on observations at the Winfield Lock and Dam experimental impact study (Barker et al. in press). Relative to the rigid cell, the thrust block is substantially less massive and has at least minimal potential to affect the response of the flexible wall system. Consequently, each thrust block is modeled with deformable solid elements (Figure 3.5b) that have an elastic concrete material model with a modulus of elasticity of 4030 ksi and a unit weight of 150 lb/ft^3. Each thrust block is merged with the corresponding rigid cell at coincident nodal locations between the bottom face of the thrust block and the top face of the rigid cell. Nodal merging provides a perfect bond between the rigid cell and thrust block, reflecting the cast-in-place construction of the foundation.

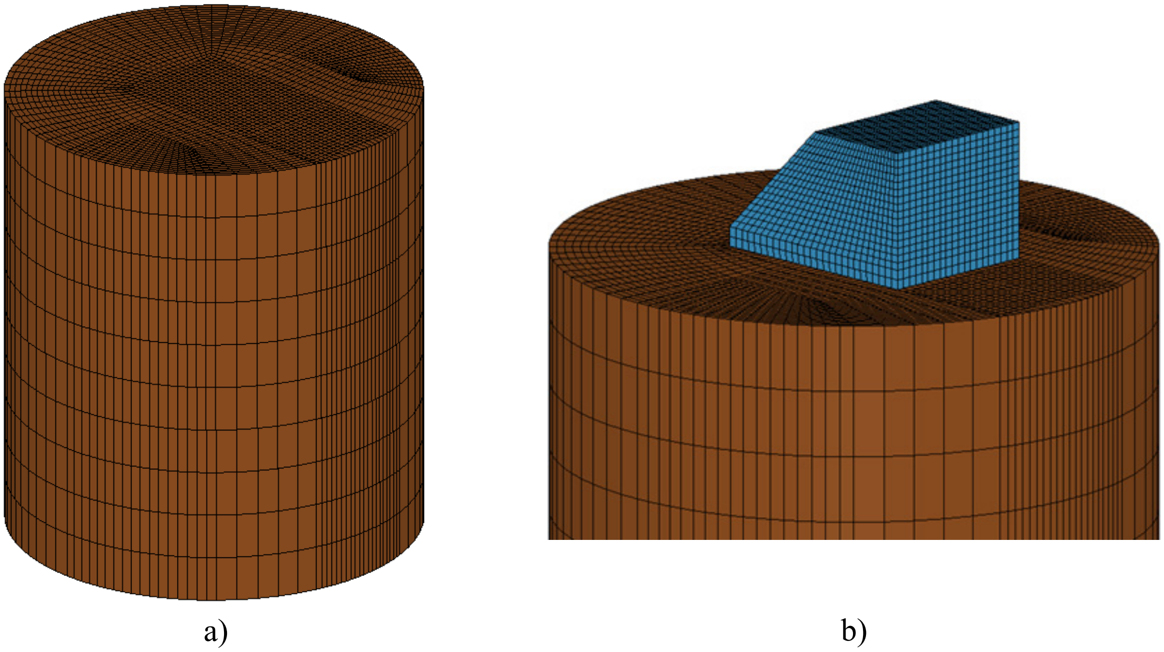
a) b)

Figure 3.5. Rendering of foundation finite element model:
a) Rigid cell; b) Thrust block attached to rigid cell

At each foundation, the flexible wall is connected to a thrust block and rigid cell by four bearing pads and two tieback anchors (recall Figure 3.4). Of the four bearing pads, two are located on the rigid cell, which resist gravity loads from the flexible wall; the two remaining bearing pads are positioned on the thrust block and transfer impact loads from the flexible wall to the thrust block. Furthermore, two tieback anchors extend from the thrust block into the flexible wall, preventing the flexible wall from "walking" off of the foundation.

Each bearing pad is modeled as a grid of discrete spring elements distributed over the footprint of the pad in the finite element mesh. Each discrete spring is assigned a stiffness corresponding to the tributary area of the bearing pad it represents (in both shear and axial modes) such that the summed stiffness of all tributary discrete springs represents the stiffness of the overall bearing pad. An illustration of this process is shown in Figure 3.6, in which the footprint of the two gravity load bearing pads is superimposed on the FE mesh of the rigid cell.

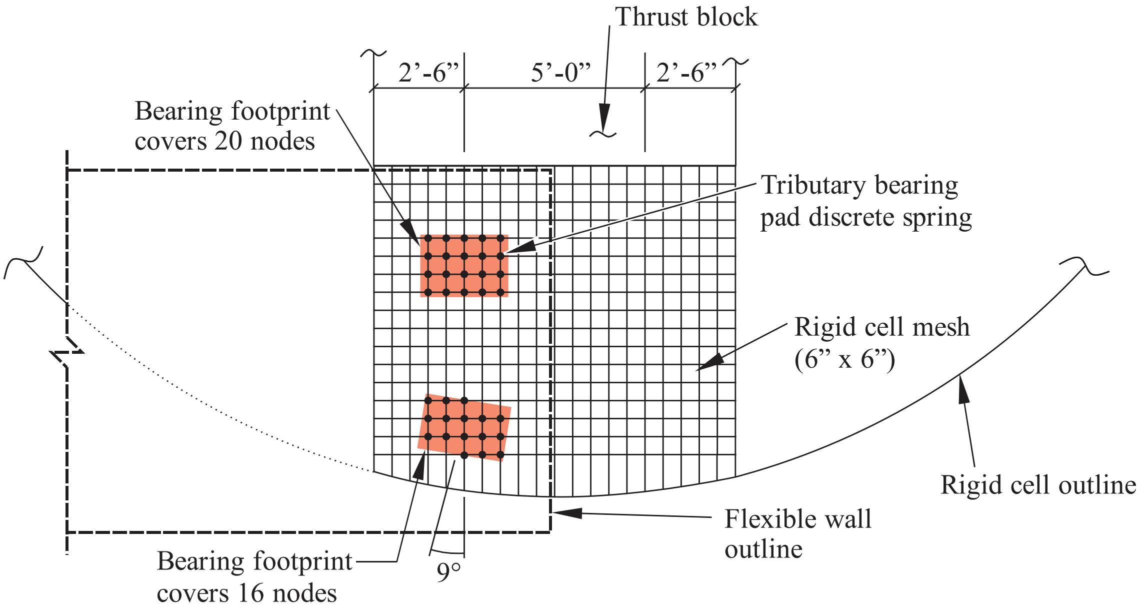

Figure 3.6. Gravity load bearing pad footprints superimposed on rigid cell FE mesh

Gravity load bearing pads on the rigid cell each have a footprint of 1 ft 6 in. by 2 ft 4 in. The thrust block bearing pad has a footprint of 1 ft 4 in. by 3 ft 6 in. and the stop block bearing pad has a footprint of 10 in. by 2 ft 2 in. All bearing pads have a 2 in. thickness with a total of three internal 14 gauge steel layers suspended in an elastomer with a durometer hardness of 50. Stiffness values are calculated for each bearing pad using the method described by Gent (2001). Computed values of overall bearing pad stiffness are given in Table 3.1. Note that these are not the values applied to individual discrete springs. Since the springs work in parallel, the stiffness values shown in Table 3.1 are divided by the number of springs in the bearing pad to calculate tributary stiffness values. In addition, axial bearing pad springs are defined such that they act in compression only and any displacements resulting in "tension" instead produce zero force between connected elements (thereby modeling gap formation between the connected elements).

Table 3.1. Bearing pad stiffness values

	Axial stiffness (kip/in)	Shear stiffness (kip/in)
Gravity bearing	13339	27
Thrust block bearing	18920	36
Stop block bearing	3807	14

Tieback anchors are modeled using a "cable" beam element within LS-DYNA. "Cable" elements are unique beam elements that can be prescribed a specified internal force level over a given time period. A cable element formulation is necessary for dealing with issues related to the staged construction of the wall system, which will be discussed later in the chapter. Each tieback anchor is a 1.375 in. diameter thread bar and is modeled with an elastic steel material model having a modulus of elasticity of 29000 ksi. Tieback anchors are debonded through their entire length; therefore, each is modeled such that only the nodes at either end of the tieback are connected to the thrust block and flexible wall.

3.3 Development of flexible wall finite element model

3.3.1 Overview of modeling approach

The flexible wall is a post-tensioned segmental concrete system spanning 118 ft between two foundation supports. Over the total span, the wall is divided into three equal length match-cast segments within which three unique cross-sectional shapes are used. A solid cross section, hollow cross section, and transition cross section (from solid to hollow) are all present in the two outer segments of the flexible wall. Within the single inner segment, only the hollow cross section is used.

To accurately capture the nonlinear behavior of the flexible wall, but to remain computationally efficient, it becomes infeasible to model the entire flexible guidance structure using three-dimensional solid continuum elements. Therefore, a hybrid approach (Figure 3.7) is instead taken with modeling the flexible wall. A combination of solid elements (used near the foundation supports) and nonlinear beam elements (used in the interior portion of the span) are used to represent the structural properties of the concrete within the flexible wall.

In addition to modeling the concrete portions of the wall, two types of steel reinforcement are modeled: mild steel bars and high strength multi-strand post-tensioned tendons. Each steel bar and tendon is modeled using a series of discrete beam elements located throughout the entire length of the flexible wall system (in both the solid element and beam element model zones). All reinforcement details and the shape of the concrete cross section are both modeled according to plan sets acquired from the USACE for the Winfield Lock and Dam.

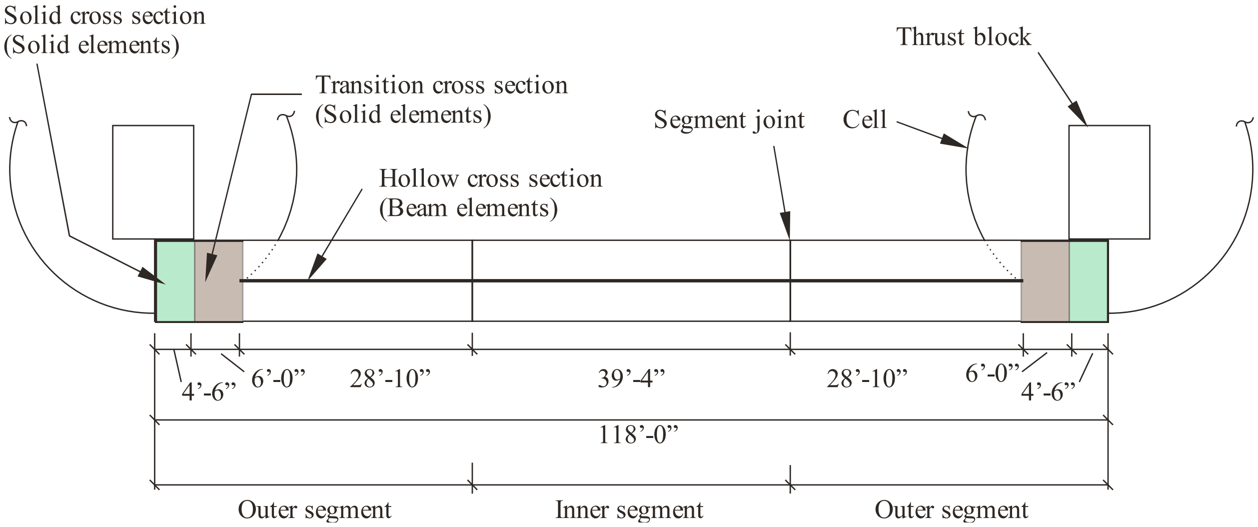

Figure 3.7. Hybrid modeling approach using both solid elements and beam elements

3.3.2 Reinforcement

Mild steel and post-tensioned multi-strand tendons are located within the wall unit as indicated in Figure 3.8. Mild steel consists of #5 and #9 reinforcing bars (rebar). Post-tensioned multi-strand tendons are comprised of varying arrangements of ½ in. diameter 270 ksi low-relaxation 7-wire strands. Each piece of mild steel reinforcement in the flexible wall is modeled separately as an individual discrete beam element, and each multi-strand tendon is represented by a single beam element having an area equal to the summation of all strand areas present within the tendon. Note that only longitudinal steel within the wall has been modeled; shear reinforcement is not included in the model.

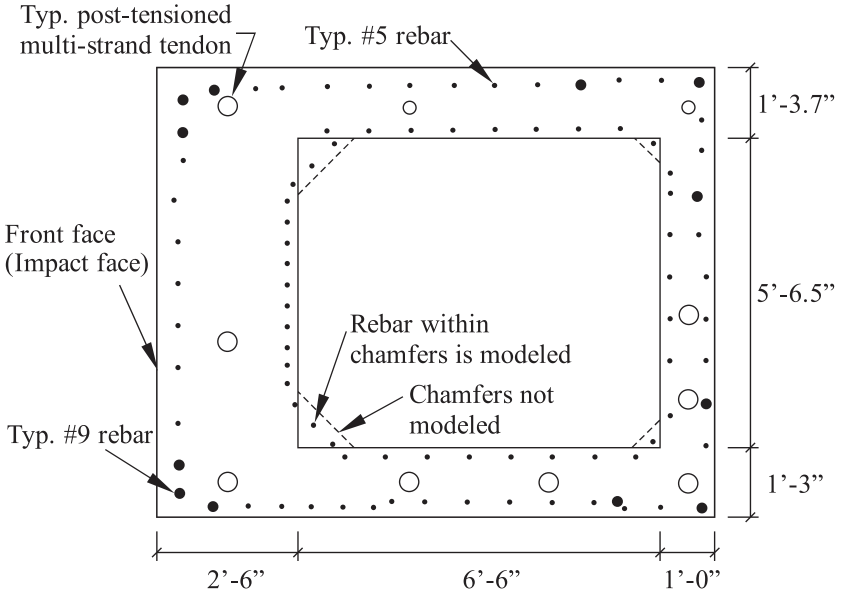

Figure 3.8. Pattern of steel reinforcement within concrete cross-section

Each steel bar and tendon within the cross section is discretized into 6 in. long elements along the entire length (118 ft) of the flexible wall. At each of the two joints where the precast concrete segments meet, the post-tensioned tendons are modeled as continuous across the joint, but the rebar elements are discontinuous (i.e., rebar elements terminate at each end of the precast segments). For mild steel rebar, the pattern of the reinforcement remains the same throughout the entire span length. However, the post-tensioned tendon profile varies within the solid and transition cross section zones. A schematic showing the tendon layout within the solid and hollow cross sections is provided in Figure 3.9. Within the transition zone between the solid and hollow cross sections, the tendon profile is assumed to change linearly between the layouts shown in Figure 3.9. Multi-strand tendon cross-sectional areas and post-tensioning forces, as noted from the structural wall plans, are provided in Table 3.2.

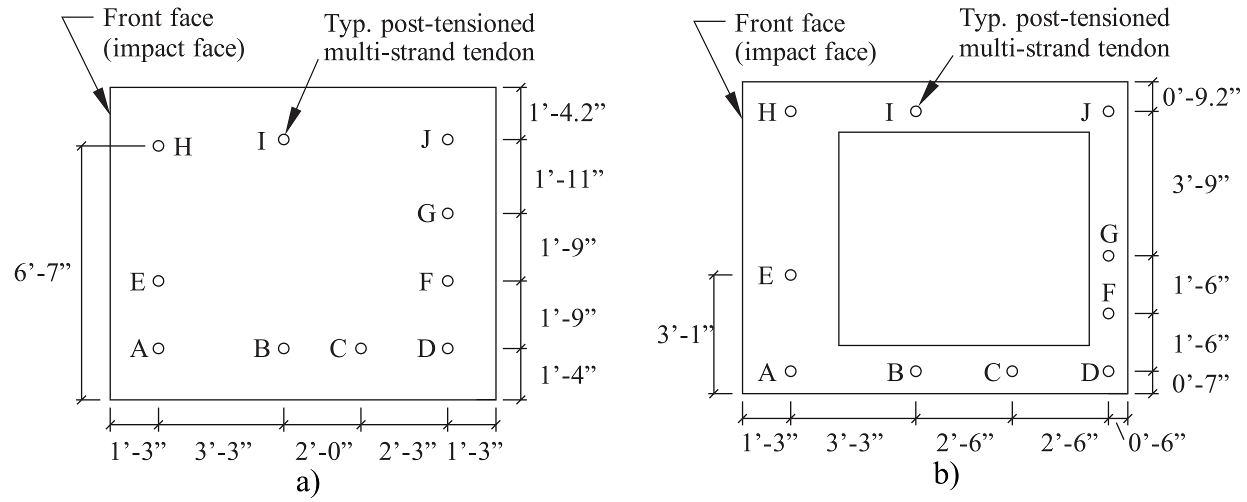

Figure 3.9. Post-tensioned tendon locations:
a) Solid cross section at ends of wall; b) Hollow cross section used throughout the interior portion of the wall

Table 3.2. Post-tensioned tendon parameters

Tendon location	No. of strands	Tendon area (in^2)	Post-tension force (kip)
A	31	4.743	747.0
B	31	4.743	747.0
C	31	4.743	747.0
D	31	4.743	747.0
E	24	3.672	578.3
F	31	4.743	747.0
G	31	4.743	747.0
H	24	3.672	578.3
I	12	1.836	289.2
J	12	1.836	289.2
Σ	258	39.474	6217

Mild steel reinforcement bars are modeled with an elastic, perfectly plastic material model, with a modulus of elasticity of 29000 ksi and a yield stress of 60 ksi. Post-tensioning strands are given a nonlinear material model corresponding to the Ramberg-Osgood function:

$$\sigma = E_p \varepsilon \left(A + \frac{1-A}{\left(1+\left(B\varepsilon\right)^{1/C}\right)} \right) \leq \sigma_{pu} \tag{3.1}$$

suggested by Collins and Mitchell (1991) for 270 ksi low-relaxation 7-wire strands. This function is illustrated in Figure 3.10. For the Ramberg-Osgood function, E_p is the strand modulus (28500 ksi) and A, B, and C are material-based constants (0.025, 118, and 10, respectively for 270 ksi low-relaxation 7-wire strands). Once the function reaches the ultimate strand stress (σ_{pu} = 270 ksi), the response becomes perfectly plastic for all larger strains.

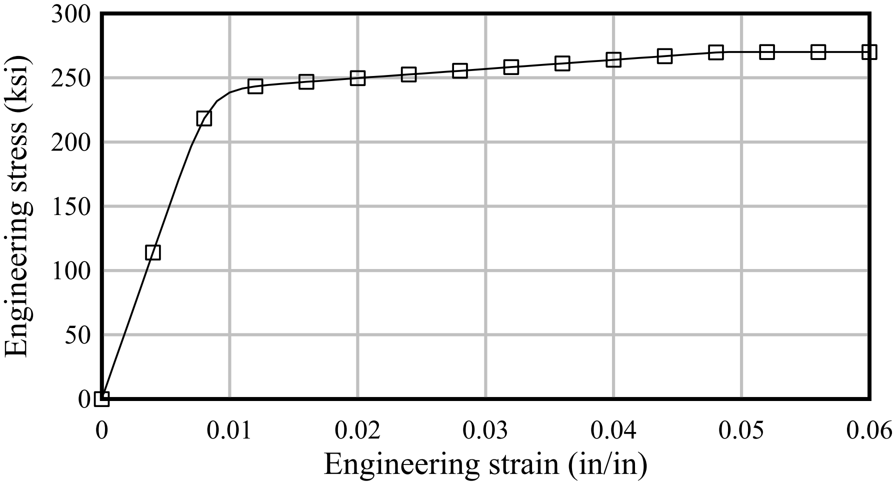

Figure 3.10. Post-tensioned tendon material model

3.3.3 Concrete solid elements

Each end segment of the flexible wall system is comprised of a beam element region and a solid element region. The solid element region is modeled nearest the cell and thrust block foundation supports for the purpose of facilitating connections to the tieback anchors and to the bearing pads. Two unique cross sections, both a solid cross section and a transition cross section (from solid to hollow), are modeled in this zone with the solid elements. Dimensions of the solid cross section are shown in Figure 3.11. Dimensions of the ends of the transition cross section are shown in Figure 3.12a and 3.12b with a linear variation assumed between the two schematics shown.

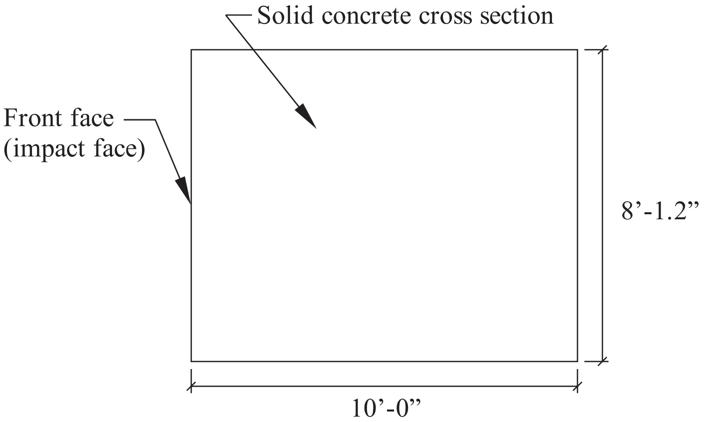

Figure 3.11. Schematic of solid cross section

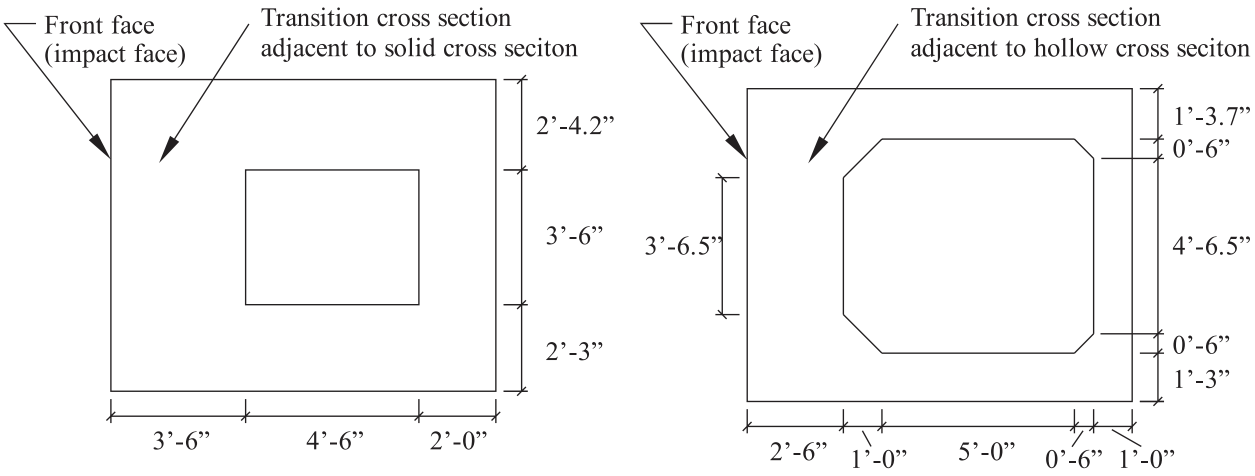

a)

b)

Figure 3.12. Schematic of transition cross section:
a) Adjacent to solid cross section; b) Adjacent to hollow cross section

For solid elements within the solid end block and transition sections of the wall, a linear elastic concrete material model is employed with a modulus of elasticity of 4030 ksi, and a unit weight of 153 pcf. Throughout most of the finite element mesh (Figure 3.13), 8-node hexahedral solid elements are used, however, 4-node tetrahedral elements are also employed in areas where the transition cross section tapers in thickness.

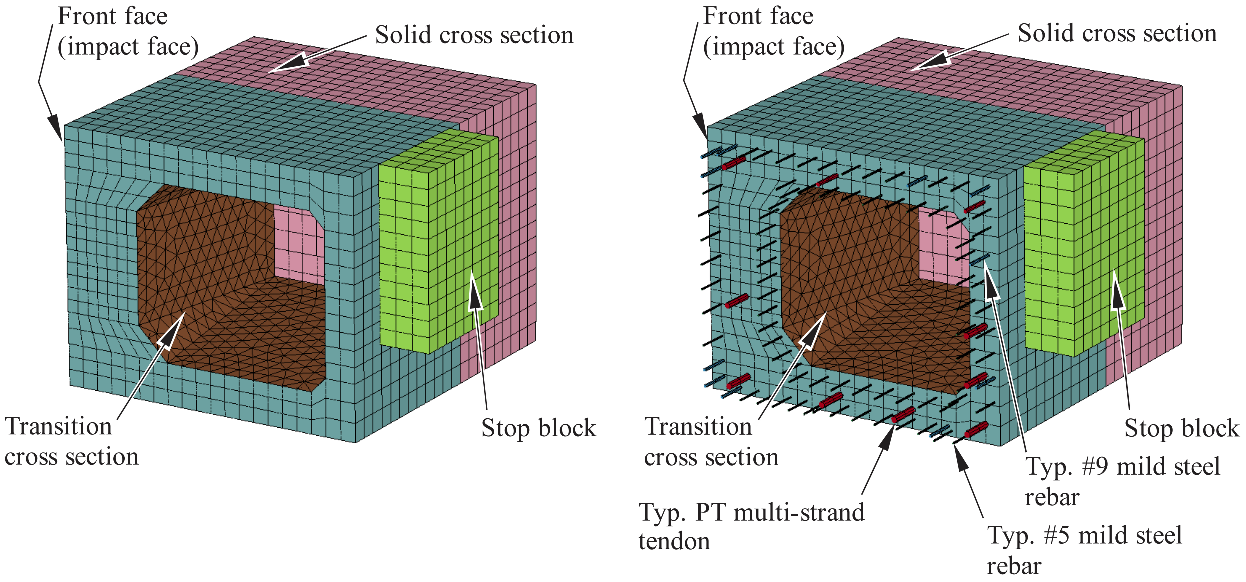

a)

b)

Figure 3.13. Rendering of solid element modeling:
a) Without reinforcement beam elements visible; b) With reinforcement beam elements visible

All solid elements in the finite element mesh are discretized so as to produce an element length of 6 in. along the length of the span. Nodal locations within the flexible wall mesh align with nodal locations in the thrust block and rigid cell meshes so that these components can be connected together using bearing pad beam elements (i.e., beam elements representing the stiffness properties of the bearing pads). Similarly, tieback anchor elements connect nodes in the thrust block solid mesh to nodes in the flexible wall solid mesh.

The 6 in. element discretization in the longitudinal direction is also important in that it permits enforcement of strain compatibility across the various components of the composite wall cross section. As is evident in Figure 3.13b, the reinforcement beam element nodes are not coincident with those of the solid elements. Without nodal coincidence (collocation of nodes), strain compatibility cannot be obtained using nodal merging. However, the nodes are all coplanar since both the reinforcement beam elements and the concrete solid elements are discretized at a 6 in. element length along the span direction of the wall. Therefore, to enforce strain compatibility in the composite wall model, a constraint set is applied to all coplanar nodes at each 6 in. cross-sectional slice of the wall. Consequently, nodes that are initially coplanar will remain coplanar (plane sections remain plane) as the cross section of the wall translates and rotates during loading.

3.3.4 Concrete beam elements

As noted earlier, the hollow portion of the flexible wall (recall Figure 3.7) is modeled with beam elements rather than with hexahedral or tetrahedral solid elements. In this mesh zone, individual beam elements, with a nonlinear material model, represent the structural behavior of each of the four faces of the concrete cross section (Figure 3.14). .

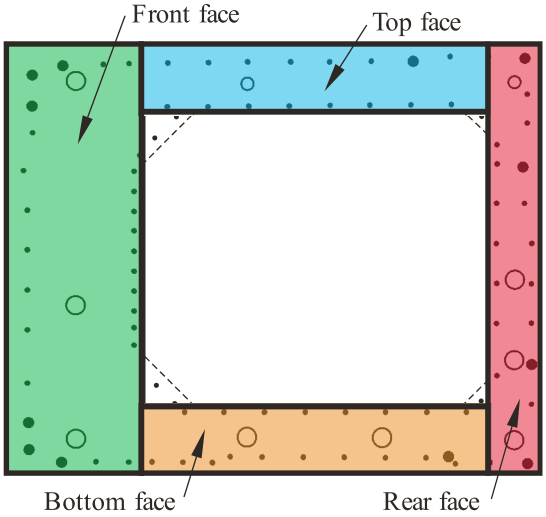

Figure 3.14. Division of hollow concrete cross section

Because each face is modeled with cross section integrated beam elements, as opposed to resultant beam elements, an arbitrary number of integration points can be specified for each rectangular ‘face beam’ in the cross section. By then specifying a large number of integration points for each face beam, a high-resolution profile of stress can be calculated for each beam element, which results in an accurate depiction of the nonlinear flexural response of the overall hollow cross section (Figure 3.15).

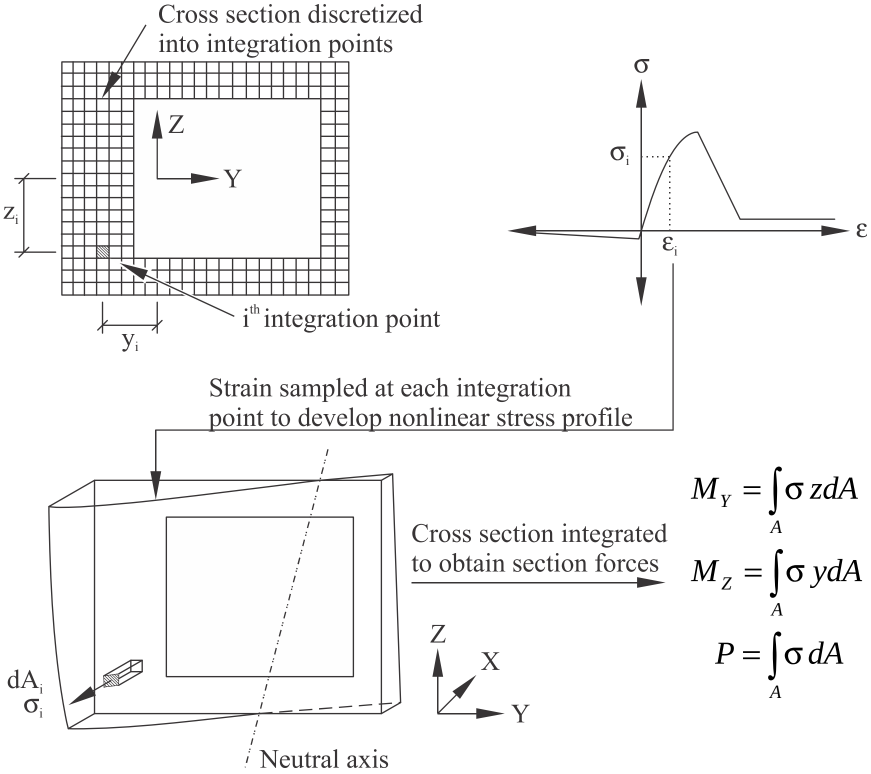

Figure 3.15. Cross section integration scheme (Depiction of integration points simplified for clarity)

Consistent with other parts of the model, each of the four face beam elements is discretized at a 6 in. element length along the span of the flexible wall. Since this element discretization coincides with that of the steel reinforcement (rebar and tendons), constraints are applied to all coplanar nodes, at every 6 in. cross-sectional slice, such that all coplanar nodes translate and rotate together (same constraint scheme as solids). This method provides strain compatibility between steel reinforcement and the concrete face beam elements and enforces the condition that plane sections remain plane.

Each face beam uses a concrete-specific material model built into LS-DYNA (LSTC 2007) in which nonlinear compressive behavior and tension-stiffening are taken into account. The LS-DYNA material model is limited, however, in that the compression curve must use the Hognestad parabola, and the tension-stiffening curve is required to be linear. Material model parameters are defined so as to target the compression model suggested by Collins and Mitchell (1991) and the tension-stiffening model suggested by Hsu (1993).

The compression portion of the target concrete material model, as suggested by Collins and Mitchell (1991) is defined by:

$$E_c = 3320\sqrt{f_c^{'}} + 6900 \tag{3.2}$$

$$n = 0.8 + \frac{f_c^{'}}{17} \tag{3.3}$$

$$\varepsilon_c^{'} = \frac{f_c^{'} n}{E_c (n-1)} \tag{3.4}$$

$$k = \begin{cases} 1 & \text{if } \varepsilon \le \varepsilon_c^{'} \\ 0.67 + (f_c^{'} / 62) & \text{if } \varepsilon > \varepsilon_c^{'} \end{cases} \tag{3.5}$$

$$\sigma_c = \left(\frac{n(\varepsilon / \varepsilon_c^{'})}{n - 1 + (\varepsilon / \varepsilon_c^{'})^{nk}} \right) f_c^{'} \tag{3.6}$$

Units for the compression model are defined in MPa for stress and modulus of elasticity. The compressive strength of concrete ($f_c^{'}$) is taken as 5 ksi (34.47 MPa), as noted on the structural wall plans provide by the USACE.

The tension portion of the target concrete material model, as suggested by Hsu (1993) is given by:

$$E_{ct} = 47\sqrt{1000 f_c^{'}} \tag{3.7}$$

$$f_{cr} = 0.00375\sqrt{1000 f_c^{'}} \tag{3.8}$$

$$\sigma_t = \begin{cases} E_{ct}\varepsilon & \text{for } \varepsilon \le \varepsilon_{cr} \\ f_{cr}\left(\varepsilon_{cr} / \varepsilon\right)^{0.4} & \text{for } \varepsilon > \varepsilon_{cr} \end{cases} \tag{3.9}$$

The cracking strain, ε_{cr}, is assumed to be 0.00008 in/in in the present study. Units for the tension model are defined in ksi for stress and modulus of elasticity. Figure 3.16 shows the resulting fit between the LS-DYNA material model and the suggested models by Hsu, Collins, and Mitchell.

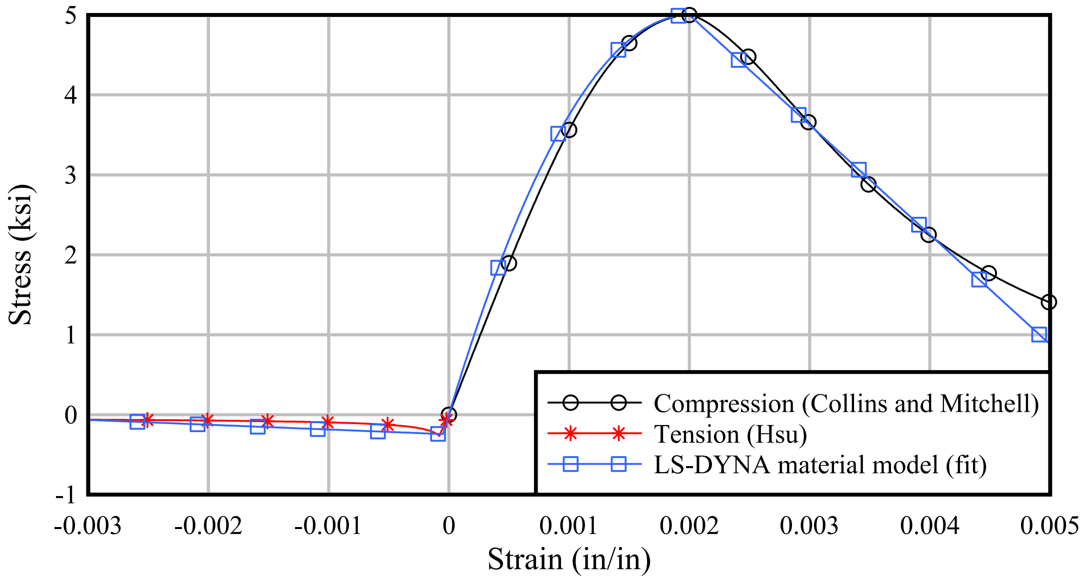

Figure 3.16. Nonlinear concrete material model fit

3.3.5 Contact shells

Since the materially nonlinear portion of the flexible wall is modeled using beam elements (as opposed to solid elements), providing the ability of the barge flotilla FE model to make contact with the beam elements (during impact) requires special modeling procedures. To create a contactable surface for the beam elements, a separate entity referred to as a contact ring is employed. A contact ring defines the perimeter surface geometry of the flexible wall, as shown in Figure 3.17, and provides a surface for the barge to contact during impact simulation.

Each contact ring is composed of a series of rigid shell elements, which together have the same physical dimensions as the perimeter of the flexible wall. Contact rings are spaced at 6 in. intervals along the axis of the flexible wall, and are 6.1 in. long (Figure 3.17) such that a small amount of overlap is provided from one contact ring to the next. Furthermore, the contact rings are spaced at 6 in. intervals so that they can be included in the constraint set between the reinforcement and concrete beam elements. Consequently, the contact rings rotate and translate with the beam elements as the wall undergoes flexural deformation.

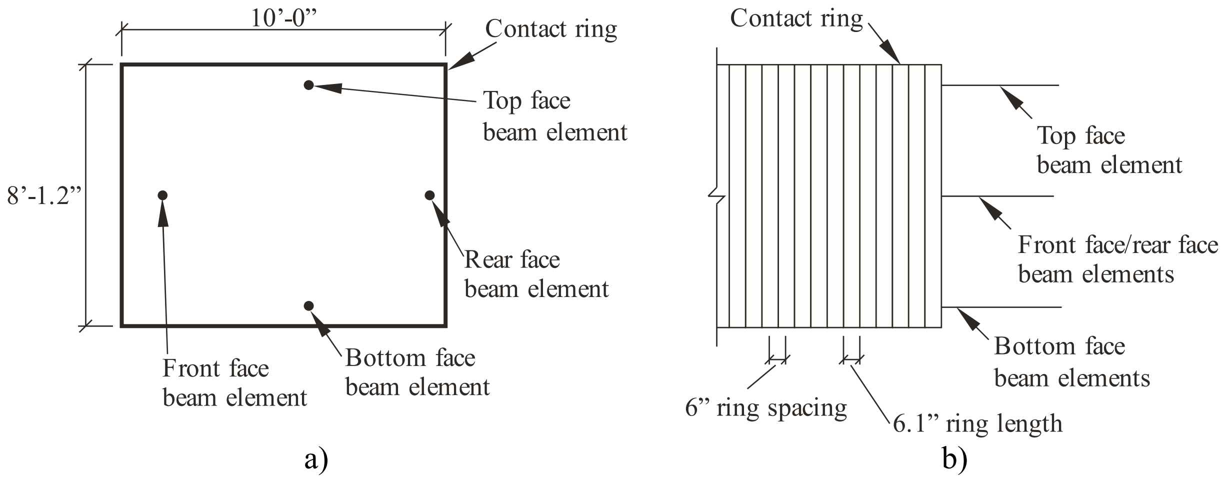

Figure 3.17. Contact ring schematic:
a) Section view; b) Elevation view (some contact rings removed for clarity)

As a barge flotilla FE model impacts the flexible wall model, contact is made directly between the surface of barge and the contact rings. Contact forces imposed on the rings are then transmitted, through the planar constraints, to the nonlinear beam elements representing both the concrete and the reinforcement. Figure 3.18 shows a schematic of this contact scheme. Note that, in the figure, only a single beam element (representative of all concrete and reinforcement beam elements) is shown for clarity of presentation.

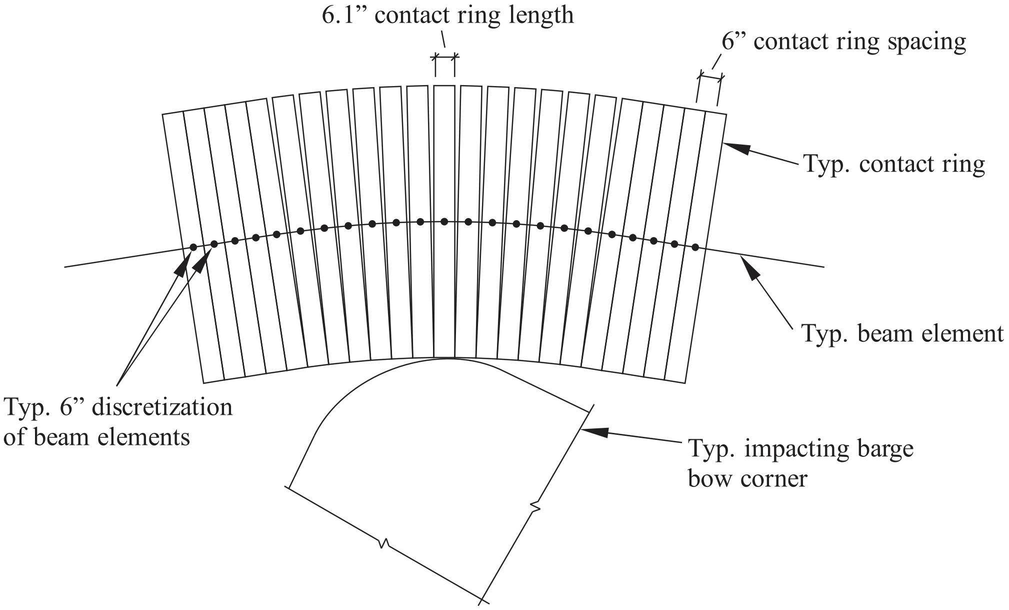

Figure 3.18. Interaction between barge and contact rings (plan view – only a single beam element shown for clarity)

While contact is defined between the impacting barge and the contact rings, contact is not defined between adjacent rings. Hence, the individual contact rings can overlap each other freely if necessary. Additionally, while the contact rings use a structural rigid material model, they are also assigned a contact stiffness equal to a modulus of elasticity of 4030 ksi (representative of concrete). Finally, since the contact rings are purely a computational mechanism used to transmit impact load, they are defined as being approximately massless so as not to adversely alter the dynamic response of the composite wall model during impact.

3.3.6 Match-cast segments

As previously discussed, the flexible wall is a segmental post-tensioned system divided into three equal length match-cast segments: two outer segments and a single inner segment. Within the outer segments, both beam elements and solid elements are employed to represent the composite concrete cross section. For the inner segment, only beam elements represent the cross section. Moreover, each of the three segments is modeled as an independent structure. Between the segments, at each segment joint, no continuity of concrete or mild steel exists. However, post-tensioning is continuous across these joints.

To model the effect of applying post-tensioning to independent segments, not only must the post-tensioning elements be modeled, but a surface at each joint for the post-tensioning to react upon must also be modeled. A rigid shell surface, referred to as the segment contact face (Figure 3.19), is modeled as the reaction surface for the post-tensioning. For each segment joint, a segment contact face is modeled on each side of the joint and has the approximate shape of the hollow wall cross section. Each segment contact face is modeled with a structural rigid material model but is given a contact stiffness (modulus of elasticity) of 4030 ksi. Contact defined between each set of adjacent segment contact faces is given a coefficient of friction of 0.6 per ACI 11.6.4.3 (ACI 2008). An initial gap of 0.001 in. is introduced between each set of adjacent segment contact faces to avoid initial contact surface penetrations at the beginning of the numerical simulation.

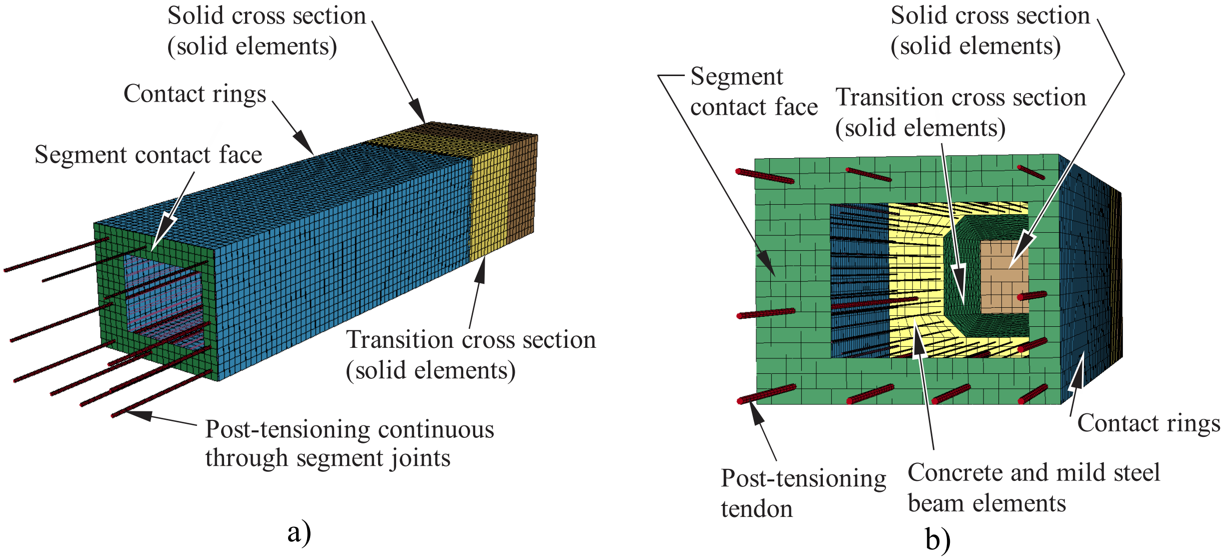

Figure 3.19. Segment contact face on outer segment of flexible wall:
a) Outer segment; b) Outer segment viewing beam element region

During extreme flexural deformation, the segment joints have the potential to form a gap on the tension side of the flexible wall, thereby inducing tension into the grout surrounding the post-tensioning at the joints. Consequently, a sensitivity study is conducted to determine the effect of debonding the post-tensioning (due to grout cracking) at the segment joints (Figure 3.20). Due to a lack of data in the literature regarding bond strength of multi-strand tendons, it is assumed that the development length of individual prestressing strands will serve as a reasonable estimate of debonded length that might result under severe cracking. The American Association of State Highway and Transportation Officials (AASHTO) suggests a development length (AASHTO 2007) of:

$$l_d \geq \kappa\left(f_{ps} - \frac{2}{3}f_{pe}\right)d_b \tag{3.10}$$

Development length is computed using the effective prestress stress (f_{pe}), the diameter of the strand (d_b), and the expected stress in the steel at nominal member resistance (f_{ps}). In addition, the FHWA has mandated a multiplier ($\kappa = 1.6$) that is applied for additional conservatism.

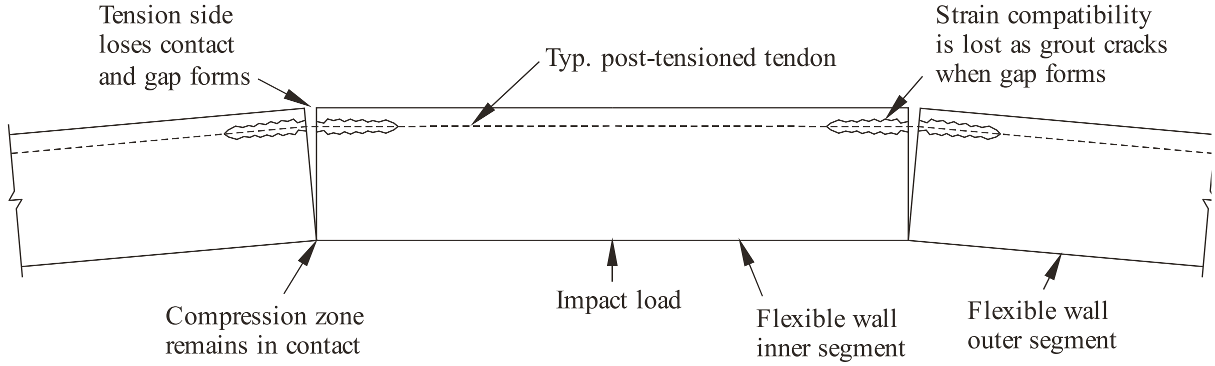

Figure 3.20. Grout cracking upon joint opening

Trial debonded lengths on each side of the segment joint, equal to the AASHTO specified development length and one-half of the AASHTO development length, are considered in the sensitivity study. Tendon debonding is modeled by removing the rotational and translational constraints between the post-tensioning elements and the concrete beam elements, thus removing strain compatibility between the tendons and the concrete. For each debonded-length case, a mid-span point load is applied quasi-statically and increased in magnitude until flexural failure of the wall occurs. Load-deflection data at mid-span, extracted from the sensitivity analysis results, are plotted in Figure 3.21. This comparison indicates that there is very little change in the response of the flexible wall for the debonding lengths tested. Furthermore, the stiffest response is provided by the non-debonded case, which would result in conservative calculation of impact forces under barge impact loading. Therefore, the flexible wall model used in this study employs no debonding of the post-tensioning at the segment joints.

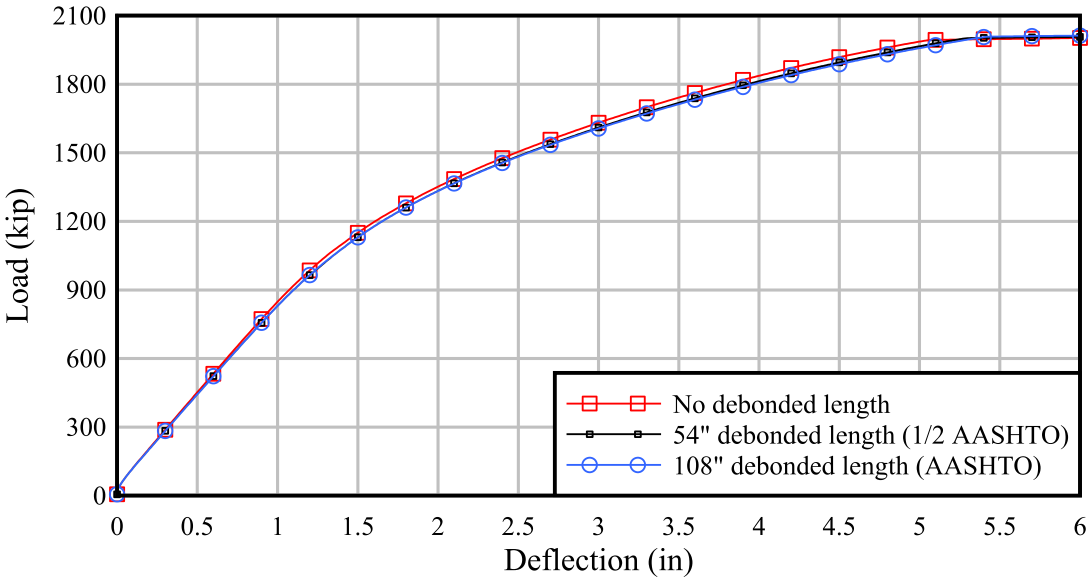

Figure 3.21. Sensitivity of debonded length of post-tensioning at segment joints

3.3.7 Flexible wall damping

Structural damping is included in the flexible wall model and, as is typical for reinforced concrete structures, a damping level of 5% of critical damping is targeted. To determine the appropriate damping parameters for use in the LS-DYNA finite element model, the concept of Rayleigh damping is considered. In the Rayleigh damping model, several modes of vibration, typically those that are most active under the loading condition of interest, are targeted to a specific level of damping. Establishing damping parameters therefore requires the identification of modes of vibration that are most active during barge impacts on the flexible wall.

To facilitate this identification, a flotilla impact simulation is conducted using the flexible wall model in order to obtain deflection time-history data. The impact condition analyzed to obtain this data involves a 3x3 barge flotilla impacting the flexible wall at mid-span with an angle of obliquity of 17° and an initial velocity of 2.9 fps. This impact condition corresponds to the highest energy test conducted during the Winfield Lock and Dam barge impact study. For this condition, the computed mid-span deflection time-history of the flexible wall is shown in Figure 3.22 (sampled at a frequency of 2000 Hz).

The deflection data presented in Figure 3.22 suggest the presence of at least two (but possibly more) active modes of vibration: an overall low frequency mode (with an approximate period of 1 sec. and frequency of 1 Hz) and a second, higher frequency mode superimposed on the lower frequency mode. To establish suitable Rayleigh coefficients for damping in the concrete wall, it is necessary to determine which modal frequencies correspond to vibrations in the wall and which correspond to unrelated oscillatory deformations in the barge flotilla. This modal separation process is carried out as follows. 1) The wall is approximated as behaving in a manner similar to a beam of uniformly distributed mass. 2) Closed-form analytical expressions are used to compute the natural frequencies of the equivalent beam representation. 3) A numerical frequency analysis is performed, using a Fast Fourier Transform (FFT), on the response data shown in Figure 3.22 to determine which of the previously analytically identified modal frequencies participate most strongly in the response of the wall to barge impact loading. 4) Once the frequencies of the key mode (or modes) of the wall that are active during impact loading have been identified, appropriate Rayleigh damping coefficients to be computed to produce the desired damping level of 5% in the wall.

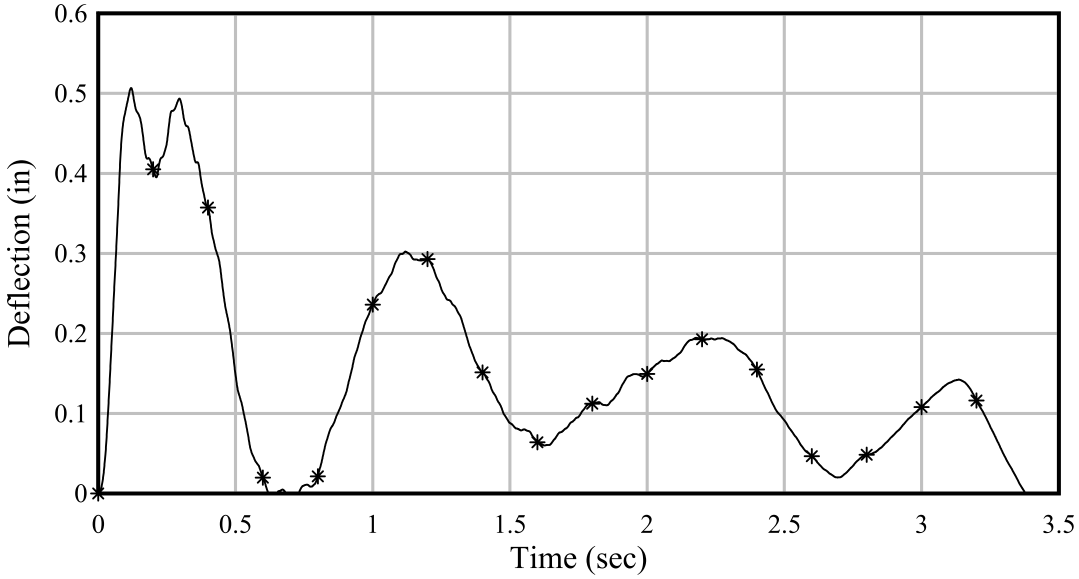

Figure 3.22. Mid-span deflection of flexible wall for 3x3 flotilla impact at 17° with initial velocity of 2.9 fps

Approximating the flexible wall as a simply supported beam with uniformly distributed mass, the natural frequencies can be calculated using the following closed-form analytical expression, as documented by Tedesco et al. (1999):

$$\omega_n = \left(\frac{n\pi}{L}\right)^2 \sqrt{\frac{EI}{\rho A}} \tag{3.11}$$

In this equation, the natural frequency (ω) is calculated for each mode (n) for span length (L), modulus of elasticity (E), moment of inertia about the desired axis of bending (I), density (ρ), and cross-sectional area (A). Using this equation, the natural frequencies of the flexible wall, for the first three modes of vibration, are 5 Hz, 21 Hz, and 47 Hz.

Figure 3.23 shows the results of an FFT analysis of the deflection data shown in Figure 3.22. Superimposed on the FFT data are the first, second, and third natural frequencies obtained by approximating the flexible wall as a simply supported beam. It is evident from Figure 3.23 that the lowest frequency content (~1Hz) in the FFT spectrum corresponds not to the wall, but to oscillations in the barge flotilla. Furthermore, for the impact condition analyzed, by far the most active wall vibration mode is the first mode: the Fourier coefficient for this mode is more than an order of magnitude larger than the coefficients for modes two or three. For this reason, only the wall mode 1 frequency is considered in calculating the concrete wall Rayleigh damping parameters for LS-DYNA.

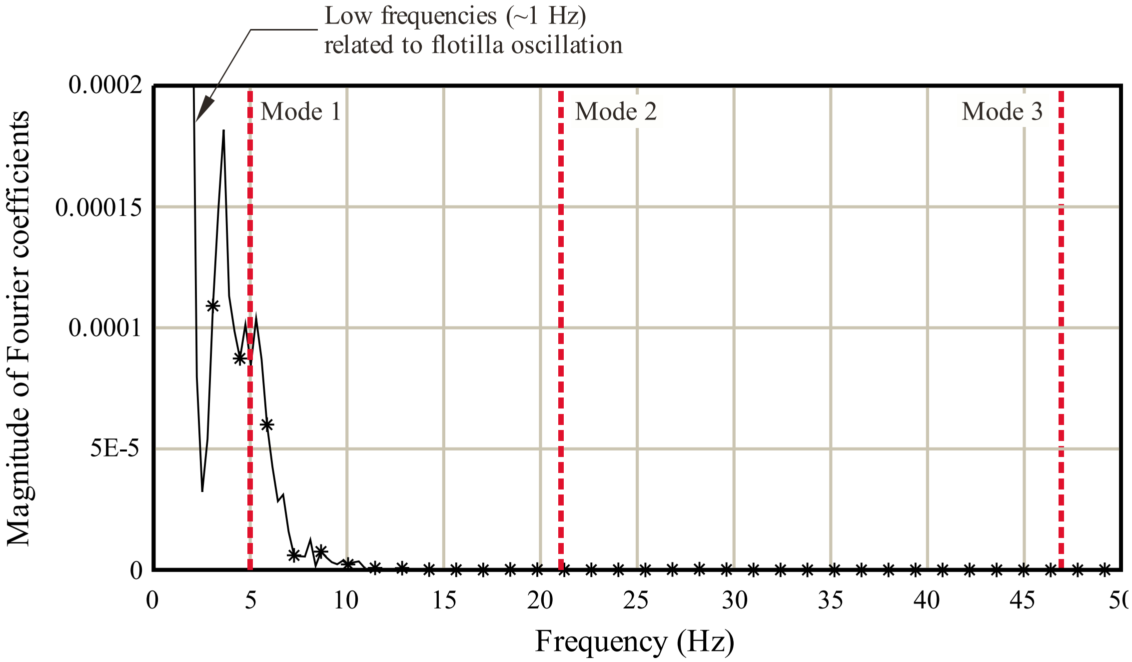

Figure 3.23. Frequency analysis of displacement time-history of flexible wall

Upon calculating the damping parameters based on achieving approximately 5% of critical damping for the first natural mode, and applying these parameters to the flexible wall finite element model, a damped free-vibration "pluck test" is numerically simulated, and the resulting deflection time-history is analyzed to verify that 5% damping exists in the model. This deflection time-history obtained from the pluck test is shown in Figure 3.24. The logarithmic decrement method:

$$\delta = \frac{1}{n}\ln\left(\frac{x_0}{x_n}\right) \tag{3.12}$$

$$\xi = \frac{1}{\sqrt{1+\left(2\pi/\delta\right)^2}} \tag{3.13}$$

is utilized to compute the damping ratio. To calculate the logarithmic decrement (δ), the magnitudes of two successively decreasing peaks are measured (where x_0 is the first peak and x_n is the second peak that is n oscillations away). Applying this calculation to the data shown in Figure 3.24 reveals that the damping is 4.9%, which is sufficiently close to the target value of 5%.

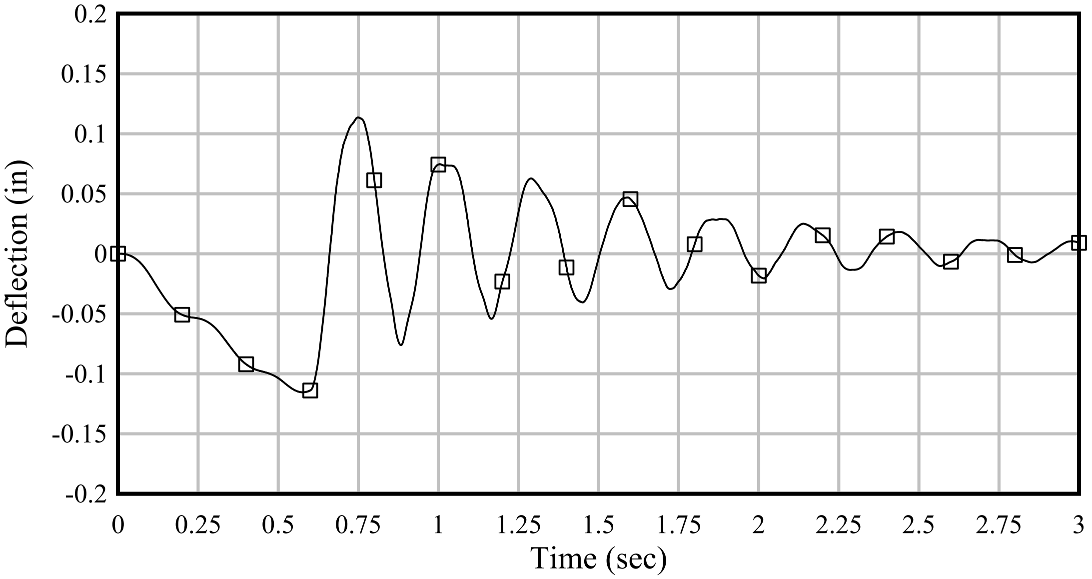

Figure 3.24. Deflection time-history for damped pluck test of flexible wall at mid-span

3.3.8 Staged construction issues and ancillary loading

Prior to subjecting the flexible wall to barge impact loading, gravity, buoyancy, and post-tensioning loading conditions must first be applied. At the construction stage where the structure has achieved static equilibrium under these load conditions, there is zero force in the tieback anchors and all bearing pads are in contact with the wall. Satisfying these prerequisites prior to conducting an impact simulation is complicated by the development of substantial elastic shortening during application of post-tensioning forces. Additionally, this elastic shortening will naturally induce forces into the tieback anchors before impact and will cause contact to be lost between the flexible wall and the stop block bearing pad. Therefore, these aspects of staged construction must be addressed to ensure that the flexible wall, under static equilibrium, will respond accurately to impact loading.

The initialization period required to apply the static loading conditions (gravity, buoyancy, and post-tensioning) and bring the beam into static equilibrium must be as short as possible to minimize computational cost. The entire initialization period, therefore, takes place over the course of one second of simulation time. For the first 0.5 sec. of this initialization period, the gravity, buoyancy, and post-tensioning loads are ramped up from 0% to 100% of their respectively defined loads. During the next 0.5 sec., the static loads are held constant and an overdamped condition is imposed on the structure to help achieve static equilibrium as rapidly as possible.

As described previously, the post-tensioned multi-strand tendon beam elements are modeled using a special formulation called “cable” beam elements. A cable element is a tension-only beam element formulation that induces a prescribed force level on the element by contracting element length through time. This behavior is particularly useful for applying post-tensioning loads to the flexible wall.

According to the USACE plan sets for the Winfield flexible wall, a post-tension force of 6217 kips is distributed through the 10 multi-strand tendons (recall Figure 3.9 and Table 3.2). In the FE model, this post-tensioning load is ramped up from t = 0 sec to t = 0.5 sec and then held constant for another 0.5 seconds (from t = 0.5 to t = 1.00 sec) while the flexible wall achieves static equilibrium (Figure 3.25). After equilibrium has been reached, the cable elements stop contracting in length, which “locks-in” the post-tension force. After this point, the elements have the ability to deform and to interact as normal beam elements, but no longer impose changes in length to introduce additional axial loads.

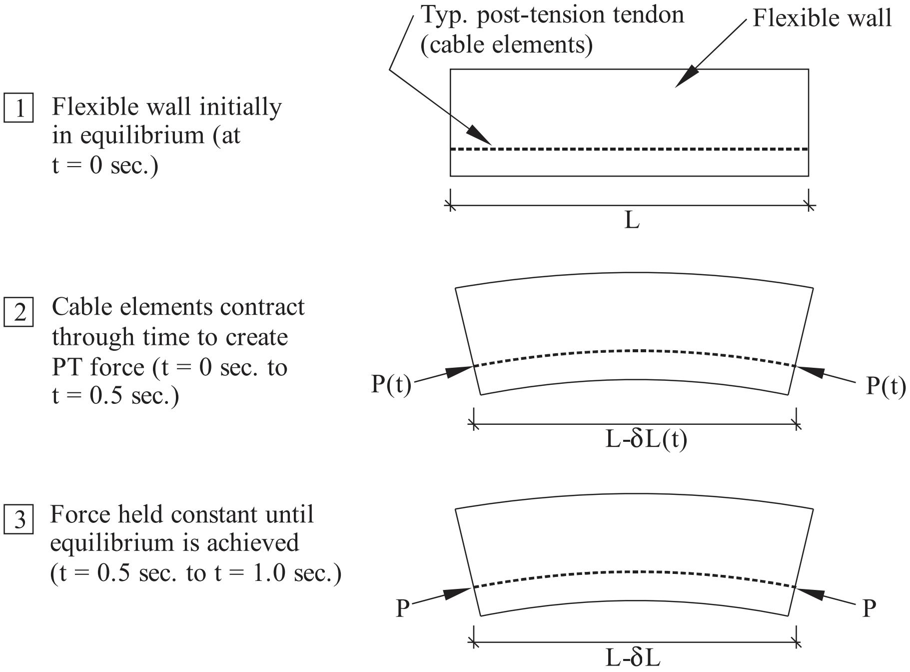

Figure 3.25. Overview of numerical process used to model post-tensioning

During application of the post-tensioning load, significant elastic shortening occurs in the flexible wall, which poses two problems. First, the shortening will introduce artificial forces into the tieback anchors; forces which would not normally occur in the actual physical structure. Second, at the stop block bearing pad, a “gap” will develop that is equal to half the length of elastic shortening of the wall. If uncorrected, upon impact by a barge, the wall will undergo a relatively large longitudinal shift (displacement) until contact between the wall and stop block bearing pad is abruptly reengaged. Again, this behavior does not correspond to the physical structure.

To solve these issues, alternative modeling techniques are utilized for each component. Each stop block bearing pad element, while present in the model, is denoted “inactive” at the beginning of the static initialization period. A time-based LS-DYNA sensor is used to “activate” each stop block bearing pad element just prior the end of the initialization period (at t = 0.99 sec.; just before impact begins). By activating the bearing pad elements in this way, each such element is considered “undeformed” at the length that results after elastic shortening of the wall has occurred. Hence, axial compressive loads applied after element activation are immediately resisted by the stiffness of the bearing pad (i.e., no gap exists).

Each tieback anchor element is treated similarly. As previously noted, the tieback anchors are modeled using “cable” beam elements. Cable beam elements–the same elements used to model post-tensioning–have the ability to contract in element length through time to achieve a specified tensile force level within the element. Since the tieback anchor elements should have zero force after static initialization (and the corresponding elastic wall shortening), a negligibly small target force level is specified during the initialization phase (from t = 0 sec to t = 0.99 sec). Consequently, the tieback anchor elements will contract or lengthen, as necessary, to achieve the specified nearly-zero target axial force level. At the end of the initialization period, the element resumes behavior as a beam element.

CHAPTER 4
VERIFICATION AND VALIDATION OF FLEXIBLE WALL MODEL

4.1 Model verification using independent cross-sectional analysis

Nonlinear flexural behavior of the flexible wall FE model is verified by comparing moment-curvature (M-Φ) data computed from the FE model to moment-curvature data calculated using an independent cross-sectional analysis tool. The cross-sectional analysis tool utilizes a numerical procedure developed by Consolazio et al. (2004) that has the capability of analyzing simultaneous biaxial bending and axial loading applied to an arbitrary concrete cross section. The procedure employs user-defined nonlinear material models for mild steel, high-strength steel, and concrete. Additionally, the procedure has been amended with the approach of Consolazio et al. (2007) to incorporate tension-stiffening into the calculation of concrete section forces.

A single span FE model (Figure 4.1) of the flexible wall is quasi-statically loaded to failure with idealized pin-roller (simple support) boundary conditions. Cross-sectional forces and section curvatures, at the mid-span of the flexible wall, are obtained from the FE simulation results data from which the moment-curvature relationship is plotted. The flexible wall FE model used in this verification case includes all nonlinear beam elements for concrete and steel reinforcement as well as solid element regions at each end of the flexible wall. However, foundation supports (cells, thrust blocks, etc.) are not modeled and the supports are instead modeled using simple pin-roller boundary conditions.

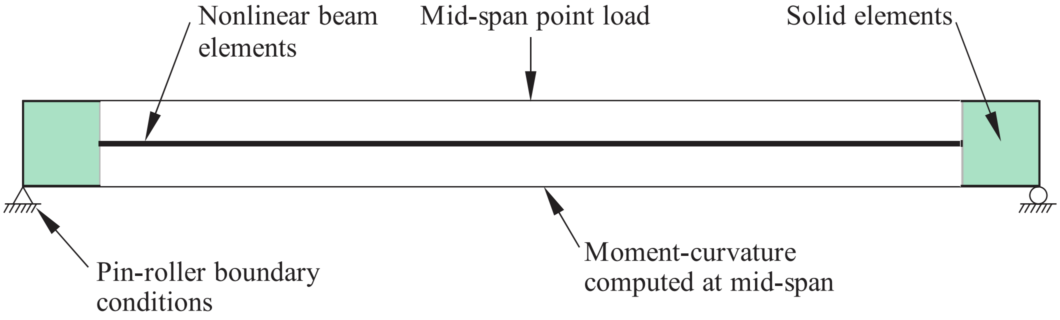

Figure 4.1. Schematic of moment-curvature FE simulation

The moment-curvature relationship for the wall is also calculated independently using a validated cross-sectional analysis software package (Consolazio et al. 2004, 2007). The concrete cross section, mild steel rebar, and post-tensioned tendons are all considered in the analysis with the appropriate nonlinear material models. A comparison of the FE and sectional-analysis moment-curvature relationships is provided in Figure 4.2. Strong agreement is observed between the cross-sectional analysis and the FE model. The ultimate moment obtained from FE analysis (631,000 kip-in) differs only by 2% from the value obtained from sectional analysis (645,000 kip-in).

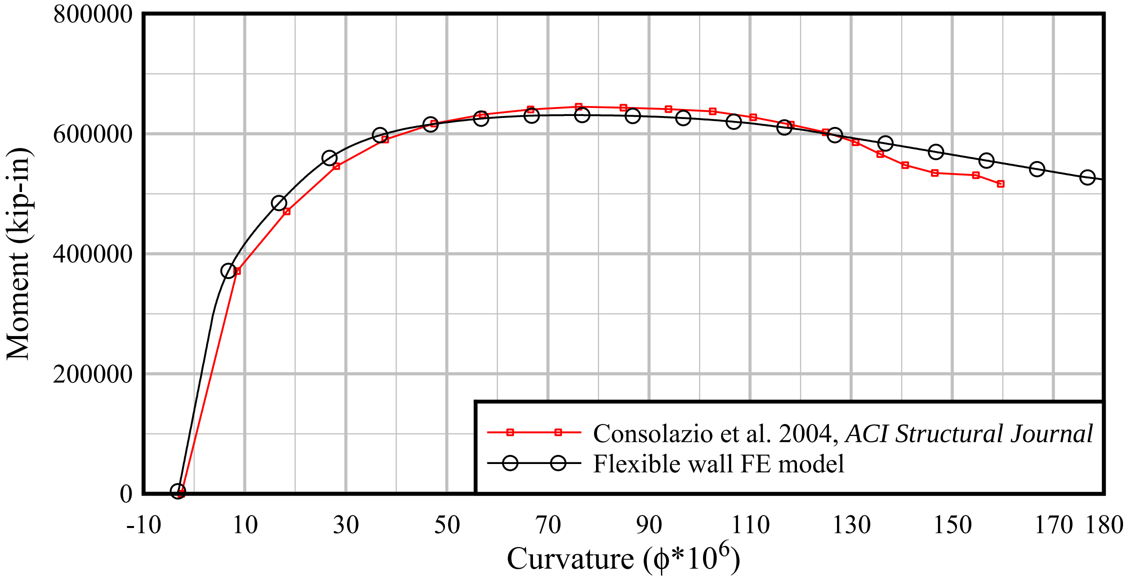

Figure 4.2. Moment-curvature relationships obtained from cross-sectional analysis and finite element analysis

4.2 Model validation using Winfield Lock and Dam experimental test data

In August 2008, the USACE conducted a series of twenty-three full-scale 3x3 barge flotilla impact experiments at the Winfield Lock and Dam in Red House, WV. As defined by the parameters illustrated in Figure 4.3, impact conditions tested at Winfield included angles of impact (θ) ranging from 5° to 20°, and impact velocities (V_0) ranging from 0.7 ft/sec (fps) to 3.6 fps. Although the final report documenting these experiments (Barker et al., in press) is still in production at the time of this writing, two measured impact force time-histories from the test program have been made available by the USACE for purposes of validating the flexible wall model developed in the present study. Impact conditions for these cases consisted of impacts by a 3x3 flotilla at: 17° with a velocity of 2.9 fps (denoted Experiment 10); and 13.6° with a velocity of 2.7 fps (denoted Experiment 20). To assess the accuracy of the flexible wall FE model, impact simulations are conducted at impact angles and velocities that correspond to Winfield impact Experiments 10 and 20.

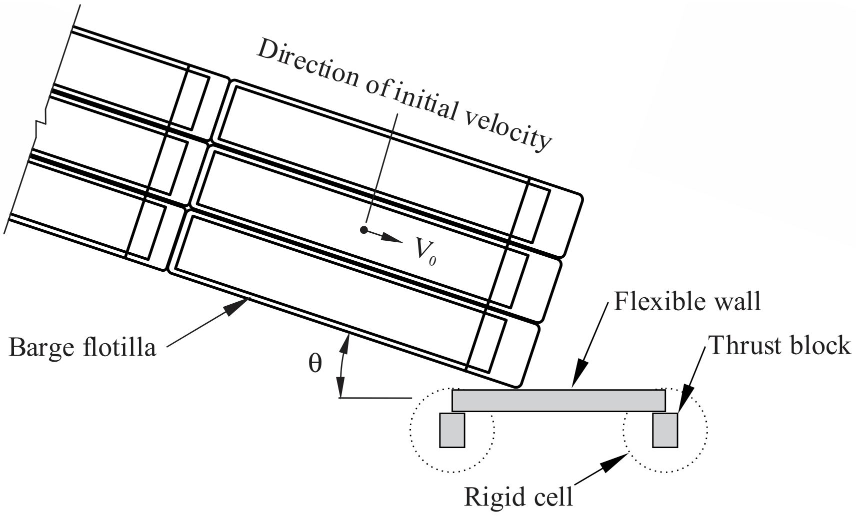

Figure 4.3. Definition of impact conditions at Winfield Lock and Dam

4.2.1 Finite element modeling of load-measurement system

Each impact experiment conducted at the Winfield Lock and Dam utilized a custom designed and fabricated load-measurement beam (Figure 4.4) attached to the corner of the impacting barge in the flotilla to quantify impact forces. The complete load-measurement system consists of a solid 9 in. x 5 in. curved steel beam, two bi-axial 400-kip clevis pin (or “shear pin”) load cells, and two clevis mounts. Each shear pin is inserted through one end of the load-beam and through a clevis mount that is welded to the barge bow. Upon impact, force is transmitted from the load beam to the shear pins, then to the clevis mounts, and finally into the corner of the barge bow. Since the structural configuration, stiffness, and distribution of impact forces associated with the load-measurement beam (and the associated pins and clevis mounts) differ substantially from those of a typical, unmodified (un-instrumented) barge corner, it is important to determine whether impact forces generated through the use of such a load beam will differ significantly from impact forces that would be generated by collision from an un-instrumented barge. If the instrumented (load-beam) and un-instrumented impact forces are significantly different, this has important implications for the design of navigation guidance structures. Furthermore, if significant differences exist, then validation of the finite element model can only achieved if a representation of the load-beam itself is included in the barge model (since this is the manner in which the experimental data were collected). Consequently, a finite element model of the load-measurement system used in the USACE impact experiments is developed for use in conducting validation impact simulations.

Figure 4.4. Load-measurement system (beam, shear pins, and clevis mounts) attached to corner of barge (Photo credit: US Army Corps of Engineers)

The FE model of the load-measurement system is shown in Figure 4.5 and is composed primarily of three-dimensional solid elements representing the two clevis mounts and the load-measurement beam. All such solid elements utilize the same nonlinear steel material model that is used in the barge finite element model (recall Figure 2.7). Other aspects of this material model include the use of a unit weight of 0.490 kip/ft^3 and the inclusion of strain rate effects.

Rather than modeling the shear pins with solid elements and using computationally expensive contact definitions between the load beam, pins, and clevis mounts, instead a series of nodal rigid bodies are used to emulate the function of the pins. A nodal rigid body in an LS-DYNA finite element model consists of a collection of nodes that are constrained to move as a single rigid body (i.e., the distances between the nodes within the body remain constant, even as the overall body translates and rotates through space).

As illustrated in Figure 4.6, at each end of the load-measurement beam, a nodal rigid body is defined to tie (constrain) nodes within the footprint of the clevis pin to a single line of nodes lying inside the clevis mount. Note that the nodal line inside the clevis mount corresponds to the hypothetical longitudinal axis of the shear pin. This modeling technique results in a computationally efficient means of allowing the end of the load beam to rotate within the clevis mesh in a way that emulates the rotation that would be permitted by a pin. For purposes of attaching the clevis mounts to the corner of the barge bow model, translational constraints are introduced between nodes on the rear faces of the clevis mounts and the nearest corresponding nodes on the bow corner plate (Figure 4.7).

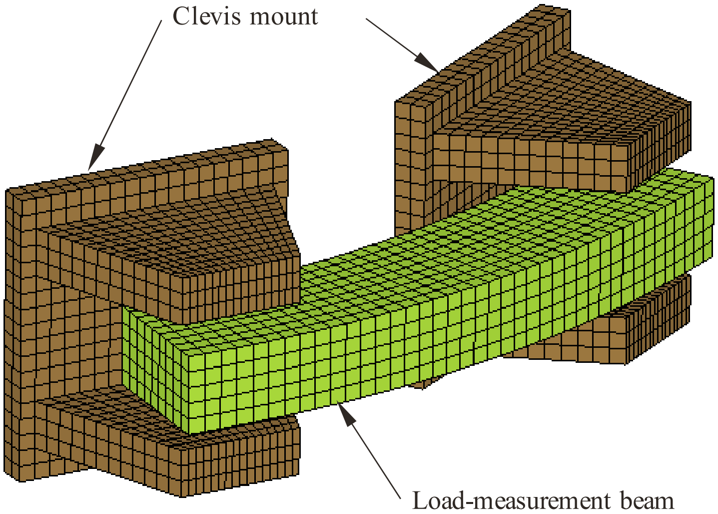

Figure 4.5. Overview of finite element model of load-measurement system

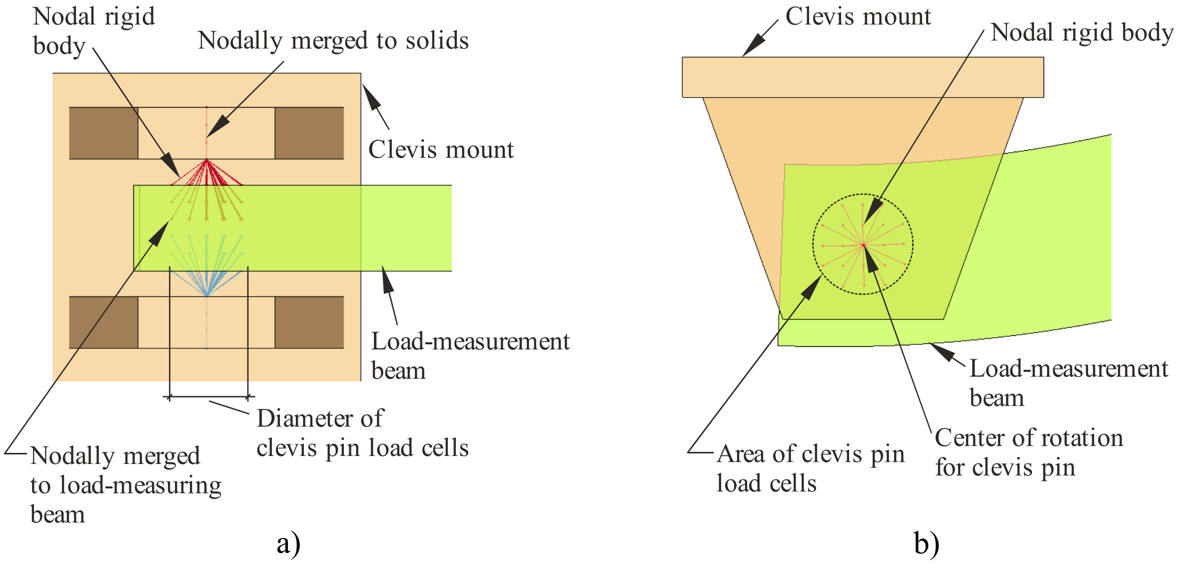

Figure 4.6. Use of nodal rigid bodies in finite element model of load-measurement system: a) Elevation view; b) Plan view

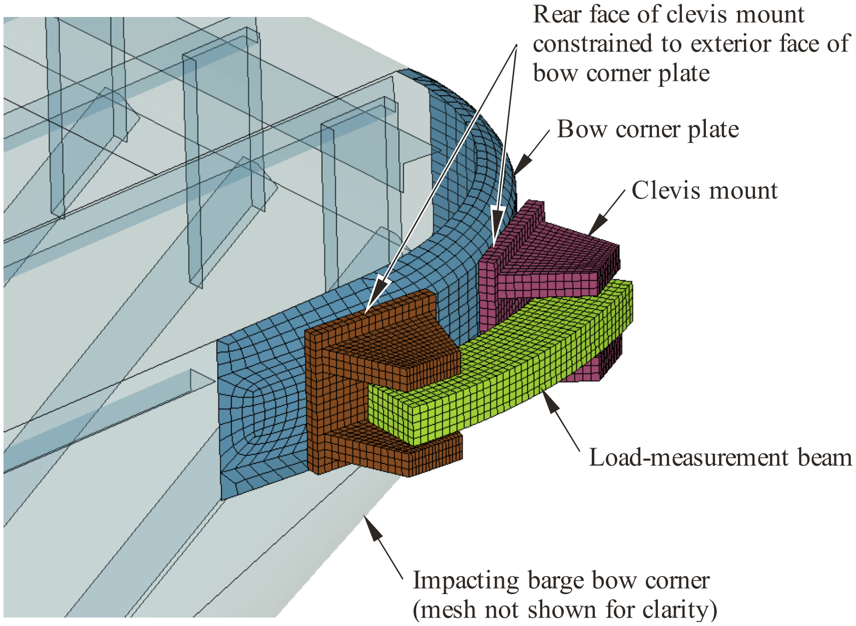

Figure 4.7. Rendering of load-measuring beam constrained to barge

4.2.2 Simulations of instrumented barge impacts on the Winfield flexible wall

To validate the flexible wall model, as well as the 3x3 barge flotilla model described earlier, simulations of impact Experiments 10 and 20 from the Winfield Lock and Dam test program are numerically simulated. As noted earlier (Section 3.3.4), information obtained from the USACE indicated that a concrete compressive strength of 5 ksi was used in the design of the wall. However, it is probable that the actual as-cast concrete strength exceeded this minimum design value. Hence, to envelope the possible range of physical test conditions, simulations of Winfield experiments 10 and 20 are conducted at both 5 ksi and 10 ksi concrete strengths (using the corresponding elastic moduli). In each simulation, the load-measurement beam discussed above is also attached to the corner of the impacting barge to replicate the experimental conditions. Comparisons of experimental data and simulation results are presented in Figure 4.8 (force) and Figure 4.9 (deflection) for Winfield Experiment 10, and Figure 4.10 (force) and Figure 4.11 (deflection) for Winfield Experiment 20. All impact force and deflection data plotted in these figures—experimental and numerical—are normal (perpendicular) to the longitudinal axis of the wall.

In Figure 4.8 (Experiment 10), the peak impact force measured experimentally, using the load-beam pictured in Figure 4.4, is 517 kips. Numerical impact simulations of the same condition, with inclusion of the load beam finite element model depicted in Figure 4.7, predict impact forces of 571 kips (5 ksi concrete) and 567 kips (10 ksi concrete)—approximately 10% more than the experimental value of 517 kips. In Figure 4.10 (Experiment 20), the peak impact force measured experimentally is 411 kips. Numerical impact simulations of the same condition predict impact forces of 448 kips (5 ksi concrete) and 461 kips (10 ksi concrete)—again, approximately 10% more than the experimental value of 411 kips.

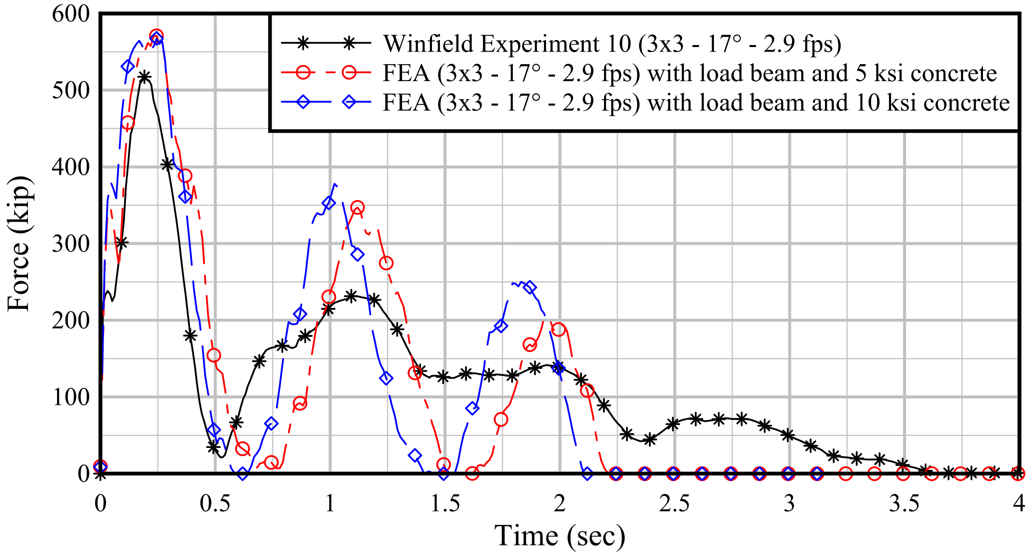

Figure 4.8. Comparison of force time-histories for Experiment 10: experimental data and finite element simulations (with load-measurement beam) for 5 ksi and 10 ksi concrete

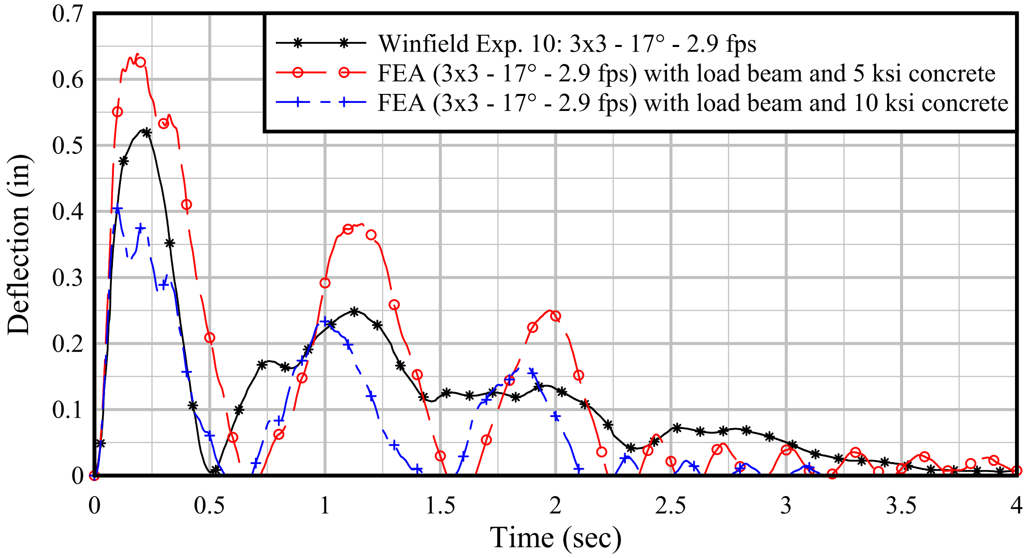

Figure 4.9. Comparison of deflection time-histories for Experiment 10: experimental data and finite element simulations (with load-measurement beam) for 5 ksi and 10 ksi concrete

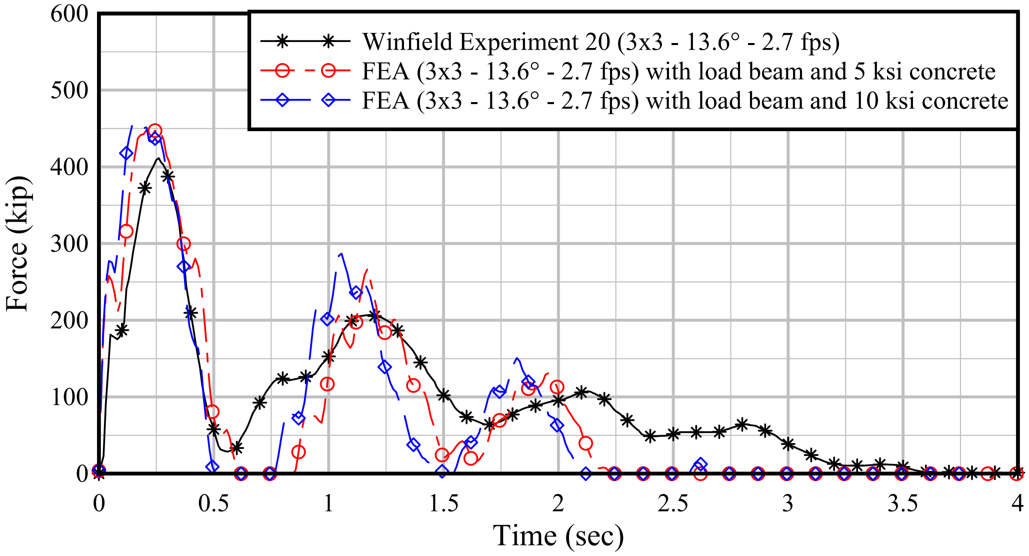

Figure 4.10. Comparison of force time-histories for Experiment 10: experimental data and finite element simulations (with load-measurement beam) for 5 ksi and 10 ksi concrete

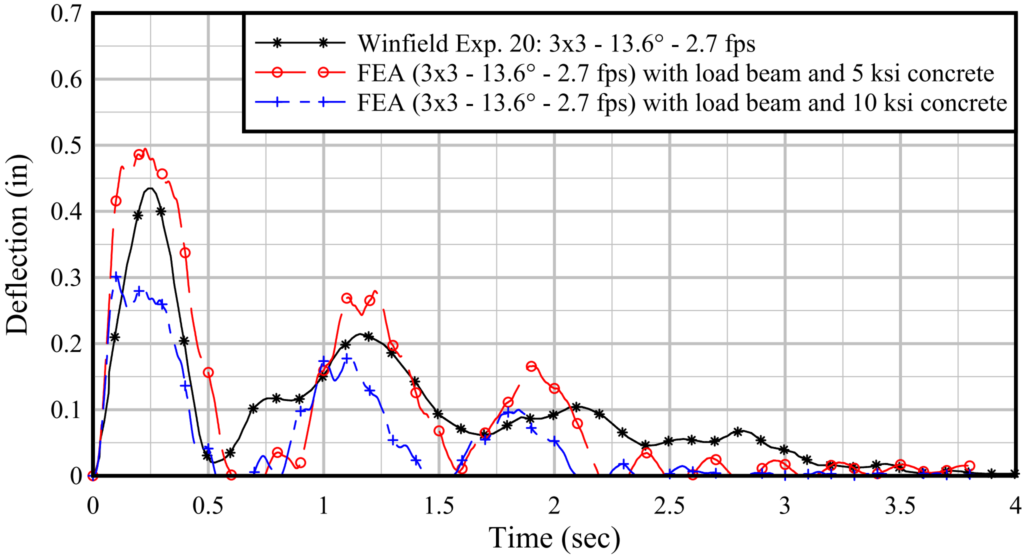

Figure 4.11. Comparison of deflection time-histories for Experiment 20: experimental data and finite element simulations (with load-measurement beam) for 5 ksi and 10 ksi concrete

Figures 4.8 and 4.10 indicate that, for the 5 ksi to 10 ksi range of strengths investigated, the modulus of the concrete wall has negligible influence on the peak impact forces. In contrast, wall deflections are considerably more sensitive to concrete modulus. In Figures 4.9 and 4.11, experimentally measured wall deflections are enveloped (bracketed) by numerical predictions utilizing 5 ksi and 10 ksi concrete strengths, and increasing the concrete modulus in each impact simulation reduces the predicted deflection (as expected). Given that the as-cast concrete strengths at Winfield were almost certainly somewhere between the bounds of 5 ksi and 10 ksi, the experimental and numerical deflection data presented in Figures 4.9 and 4.11 are considered to be agree favorably. Additionally, in Figures 4.8 through 4.11, it is noted that the dynamic *frequency* of oscillation in the experimental and numerical time histories are in reasonable agreement.

Based on the force and deflection comparisons, it is concluded that when the numerical simulation models account for the manner in which the physical tests were conducted (i.e., use of the load-measurement beam), good agreement is observed between the experimental and numerical data. Given the agreements in peak impact force, wall deflection, and oscillation frequency, the flexible wall model and the barge flotilla model are considered to be validated to a level of accuracy that is acceptable for use in this study (~10% error in predicted impact force). However, before proceeding to conduct a parametric study for the purpose of quantifying impact forces over a range of different impact conditions (next chapter), it is important to first assess any influences that the load-measurement beam may have on measured impact forces.

To carry out this assessment, the Winfield experiment 10 and 20 impact conditions are again simulated numerically, however, this time the load-measurement beam is *not* included in barge flotilla model so that the *un-instrumented* starboard corner of the barge bow—rather than the load beam—makes contact with the wall. In Figures 4.12 and 4.13 impact forces predicted with and without the load-measurement beam are compared. For experiment 10 (Figure 4.12), peak impact forces are 571 kips with the load beam (instrumented) and 426 kips without the load beam (un-instrumented). For experiment 20 (Figure 4.13), peak impact forces are 448 kips with the load beam and 353 kips without. Hence, peak impact forces predicted using an instrumented barge (with a load-measurement beam) are found to be considerably larger—approximately 20% to 25%—than corresponding forces predicted using an un-instrumented barge. This observed force increase is attributed to the fact that the stiffness of the load-measurement beam is considerably larger than the stiffness of a typical un-instrumented barge bow corner.

Importantly, this finding indicates that unnecessary conservatism could be unintentionally introduced into impact loads specified in design standards if such standards are developed strictly based on experimental forces measured using devices such as the load-measurement beam. Since the goal in the remainder of this study is to quantify peak impact forces for impacts from typical un-instrumented commercial barge flotillas, the impact simulations described in the following chapter are conducted using flotilla models (3x3 and 3x5) in which the load-measurement beam is excluded.

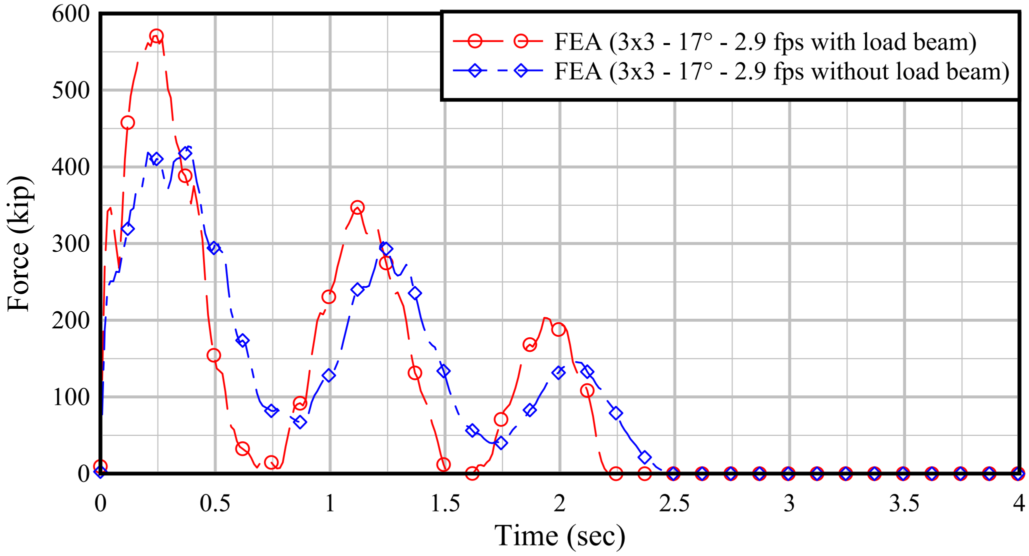

Figure 4.12. Comparison of force time-histories for Experiment 10: finite element simulations with load-measurement beam and without load beam (un-instrumented)

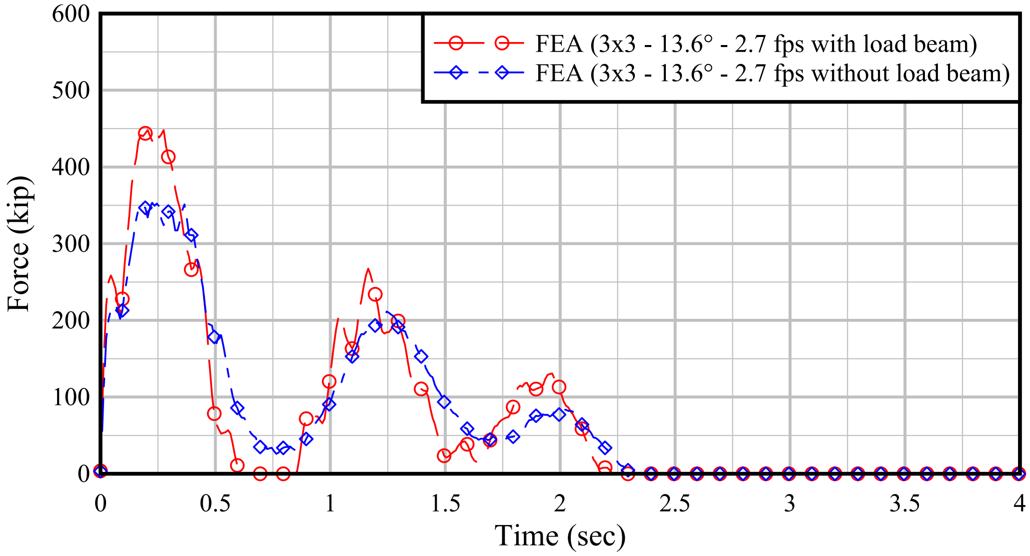

Figure 4.13. Comparison of force time-histories for Experiment 20: finite element simulations with load-measurement beam and without load beam (un-instrumented)

CHAPTER 5
IMPACT SIMULATIONS AND RESULTS

5.1 Overview

Using the barge flotilla and flexible wall finite element models verified and validated in the previous chapter, a core set of fifteen dynamic impact simulations are conducted at angles of obliquity (θ) ranging from 10° to 30° and at impact velocities (V_0) ranging from 2 fps to 5 fps with impact occurring at mid-span (Figure 5.1, Table 5.1). Each impact simulation utilizes either a 3x3 barge flotilla model (three strings of three barges each; recall Figure 2.4) or a 3x5 barge flotilla model (three strings of five barges each) to impact the high-resolution FE model of the Winfield flexible wall.

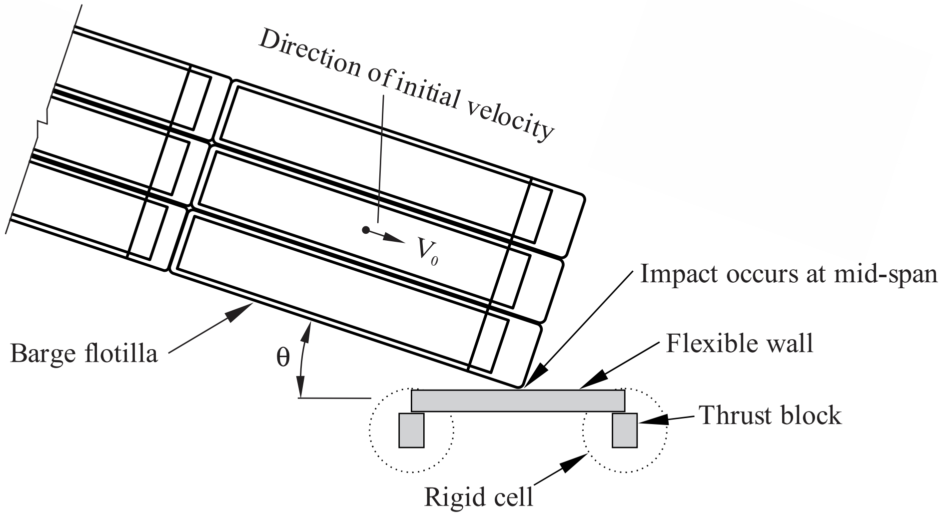

Figure 5.1. Schematic of impact condition for flotilla impact simulations

Table 5.1. Barge flotilla impact conditions

Flotilla type	Angle (θ)	Velocity (V_0) (ft/sec)
3x3	10	2
3x3	10	3
3x3	10	4
3x3	20	3
3x3	20	4
3x3	20	5
3x3	30	3
3x3	30	5
3x5	10	2
3x5	10	3
3x5	20	2
3x5	20	3
3x5	20	4
3x5	30	4
3x5	30	5

5.2 Force time-histories of impact simulations

In Figures 5.2 through 5.7, impact force time-histories are plotted for each case noted in Table 5.1. Each force plot presents results of a specific barge flotilla size and impact angle wherein the individual data traces represent different impact velocities. Forces shown are normal (perpendicular) to the impact face of the flexible wall and have not been filtered or smoothed in any way (i.e., they are 'raw' simulation results). Each impact simulation is carried out (continued) through time until both a zero impact force is achieved and the velocity vector of the flotilla indicates movement away from the flexible wall, thereby indicating impact has ceased and subsequent re-impact is extremely unlikely. Peak impact forces and peak mid-span wall deflections (resolved normal to the impact face of the wall) are summarized in Tables 5.2 and 5.3 for each flotilla size (3x3 and 3x5).

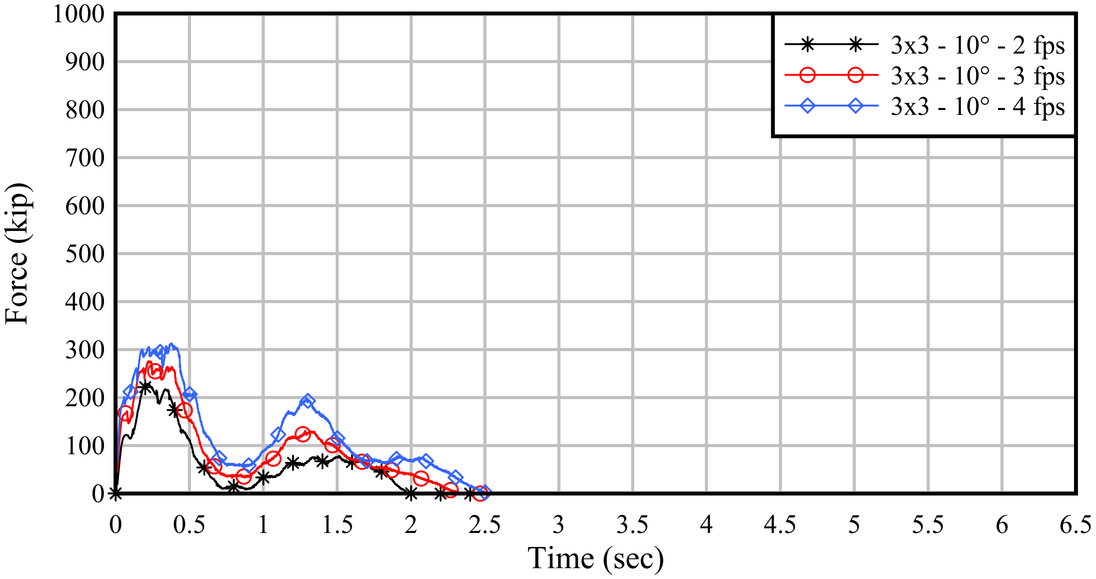

Figure 5.2. Force time-histories for 3x3 barge flotillas impacting at 10°

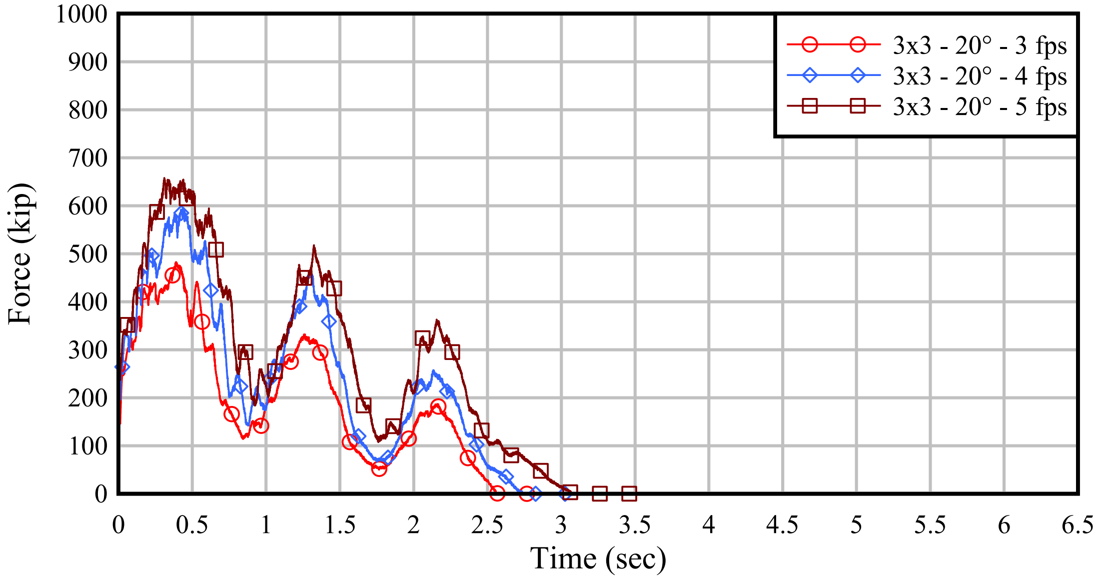

Figure 5.3. Force time-histories for 3x3 barge flotillas impacting at 20°

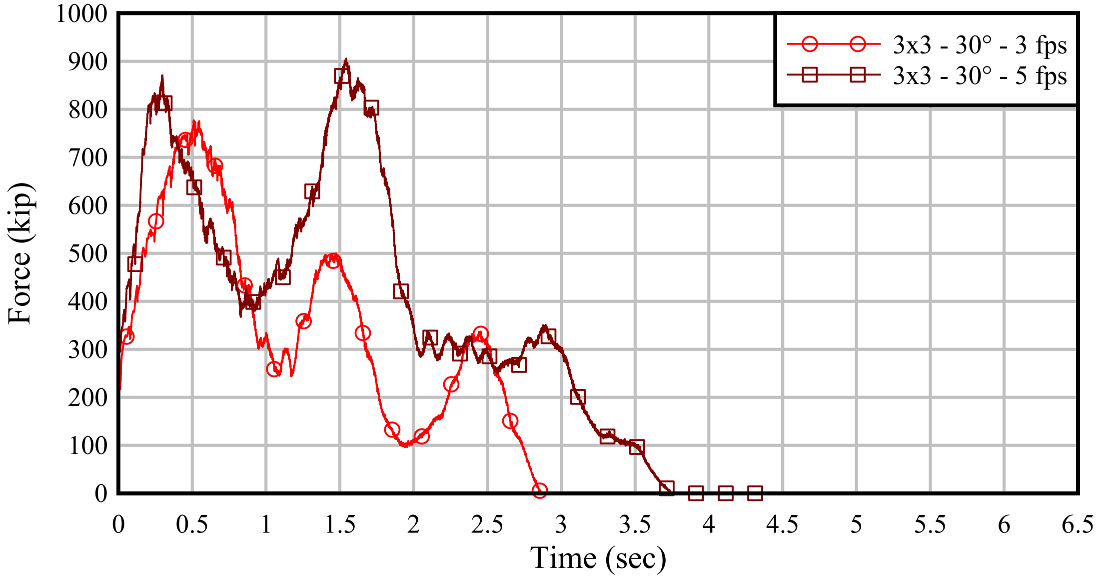

Figure 5.4. Force time-histories for 3x3 barge flotillas impacting at 30°

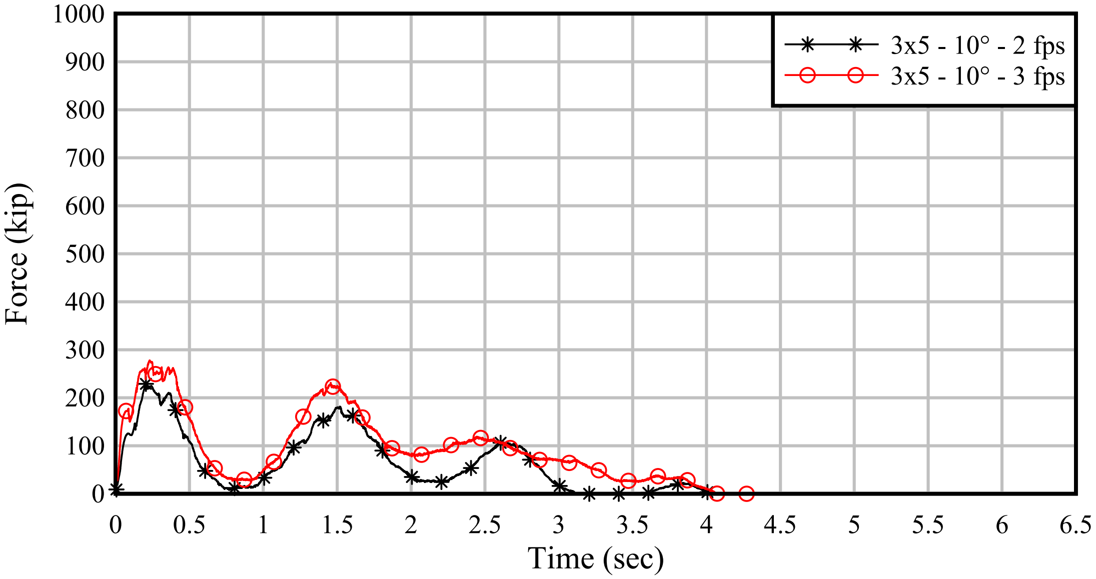

Figure 5.5. Force time-histories for 3x5 barge flotillas impacting at 10°

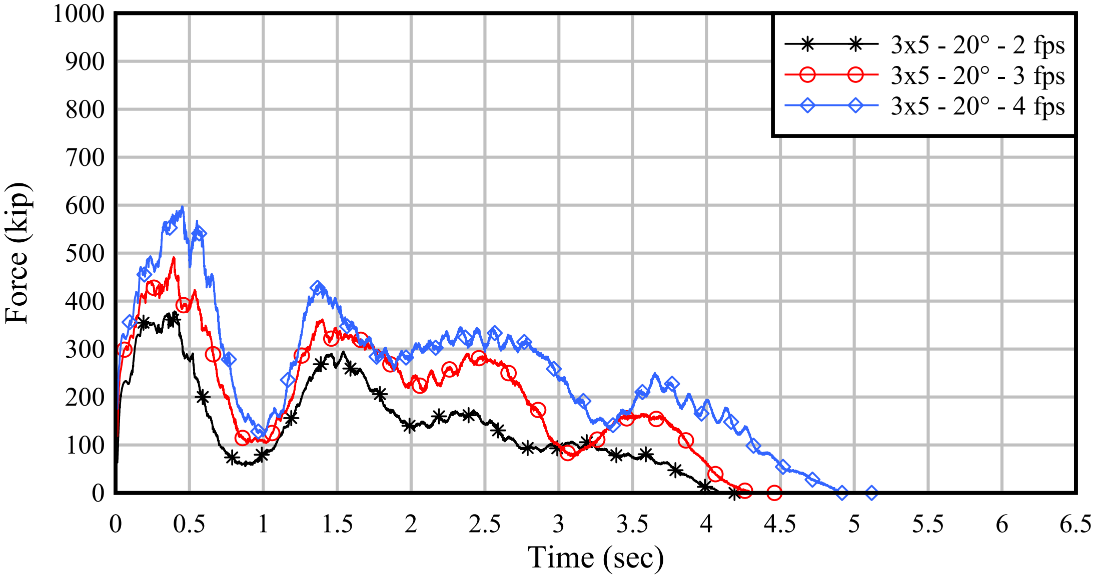

Figure 5.6. Force time-histories for 3x5 barge flotillas impacting at 20°

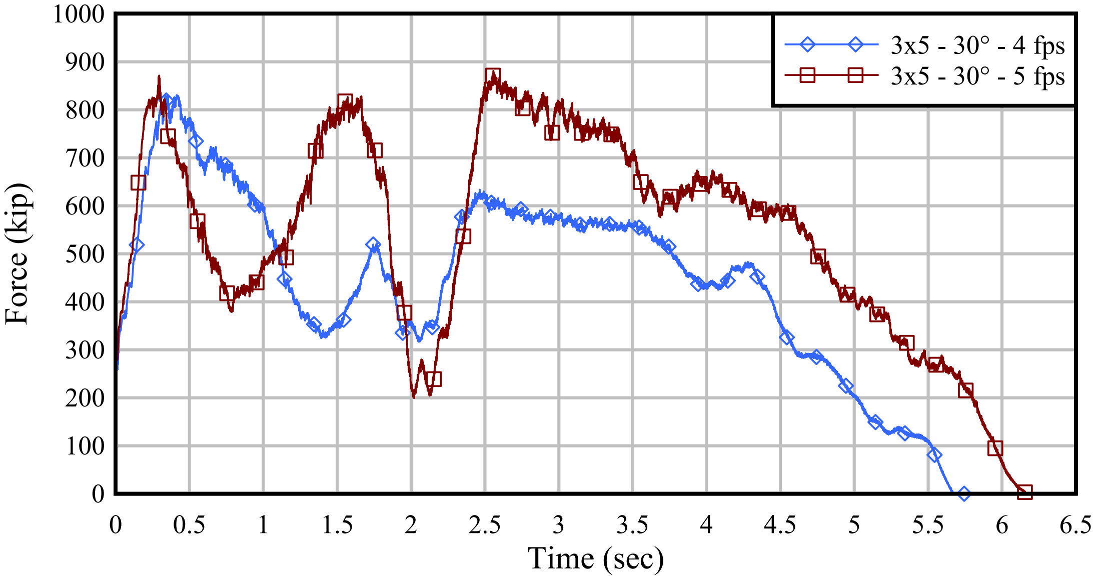

Figure 5.7. Force time-histories for 3x5 barge flotillas impacting at 30°

Table 5.2. Summary of results from 3x3 barge flotilla impact simulations

Impact condition	Peak normal impact force (kip)	Peak normal mid-span deflection (in)
10° – 2 fps	229	0.259
10° – 3 fps	276	0.313
10° – 4 fps	313	0.388
20° – 3 fps	483	0.554
20° – 4 fps	595	0.636
20° – 5 fps	658	0.735
30° – 3 fps	778	0.761
30° – 5 fps	906	0.992

Table 5.3. Summary of results from 3x5 barge flotilla impact simulations

Impact condition	Peak normal impact force (kip)	Peak normal mid-span deflection (in)
10° – 2 fps	229	0.252
10° – 3 fps	278	0.319
20° – 2 fps	378	0.439
20° – 3 fps	492	0.572
20° – 4 fps	598	0.630
30° – 4 fps	831	0.884
30° – 5 fps	881	0.965

When the data presented in Tables 5.2 and 5.3 are considered independently of each other, the trends indicated are essentially as expected in that increases of impact velocity and/or impact angle are accompanied by increases of impact force. However, when comparisons are made between impact forces generated by different barge flotilla sizes (masses) impacting under the same conditions (approach angle and impact velocity), the results are not as expected. As the data summarized in Table 5.4 demonstrate, peak impact forces produced by 3x3 and 3x5 flotilla impacts are nearly identical (less than 3% difference) as long as the impact conditions (angle, velocity) are identical.

Table 5.4. Comparison of results between 3x3 and 3x5 flotilla impact simulations

Impact condition	Normal impact force (kip)	
	3x3 flotilla	3x5 flotilla
10° – 2 fps	229	229 (+0%)
10° – 3 fps	276	278 (+1%)
20° – 3 fps	483	492 (+2%)
20° – 4 fps	595	598 (+1%)
30° – 5 fps	906	881 (-3%)

This phenomenon of increased barge flotilla size (mass) not being accompanied by increased impact force, while unexpected, can be understood by considering the longitudinal flexibility of multi-barge flotillas. A flotilla is comprised of individual barges (each with a relatively high stiffness) that are interconnected by a series of lashings (with a relatively low stiffness). In most flotilla collision scenarios, peak impact force occurs during the initial load pulse that is generated during initial contact with the wall. During this phase, only the fore-most portion of the flotilla is redirected by the flexible wall. In Figure 5.8, a simplified illustration of flotilla deformation during this phase is presented. The portion of flotilla mass effectively engaged by the wall when peak impact force is generated is essentially the same regardless of flotilla length (3x3 or 3x5).

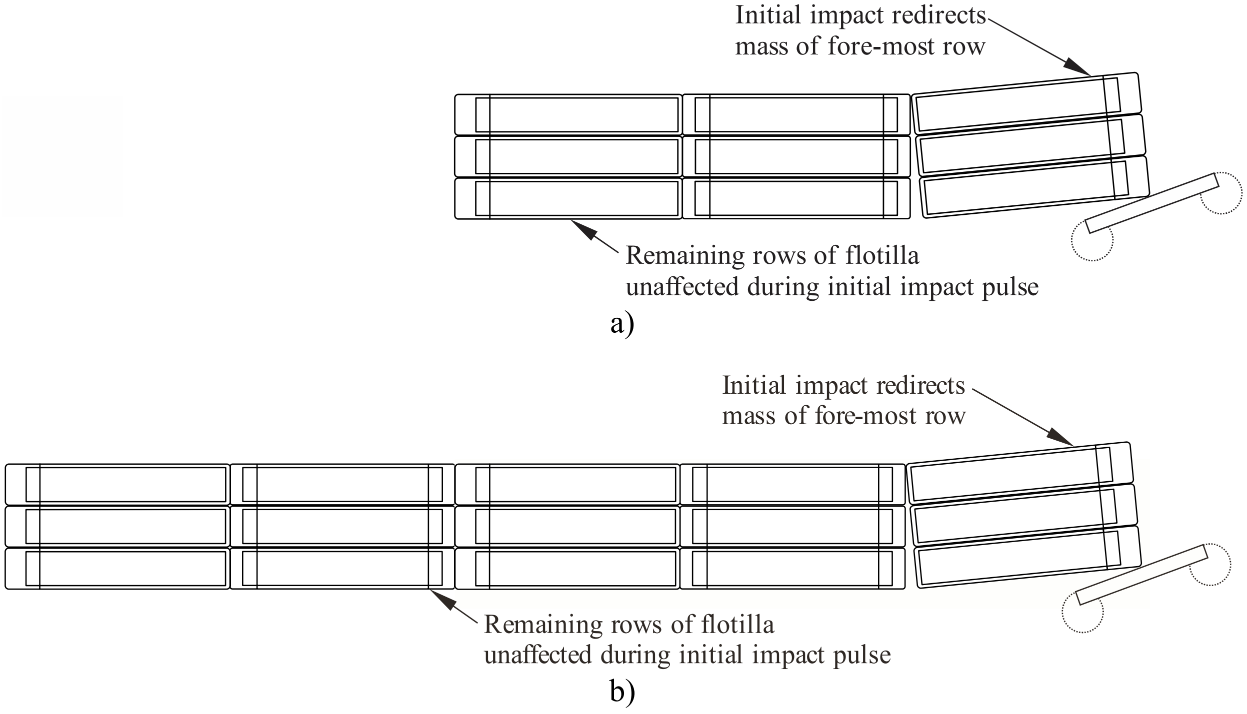

Figure 5.8. Simplified illustration of flotilla deformation during impact:
a) 3x3 barge flotilla; b) 3x5 barge flotilla

This effect is clearly evident upon examination of the finite element simulations results. Figure 5.9 shows the deformed configurations (scaled by a factor of 50 so that deflections are easily visible) of the 3x3 and 3x5 barge flotillas at time t=0.4 sec (when peak impact force occurs for the 20°, 3 fps impact condition). Clearly apparent in the figure is the fact that, at the point in time when peak impact force is generated, only the first (fore-most) row of barges has deflected in both the 3x3 and 3x5 impact cases.

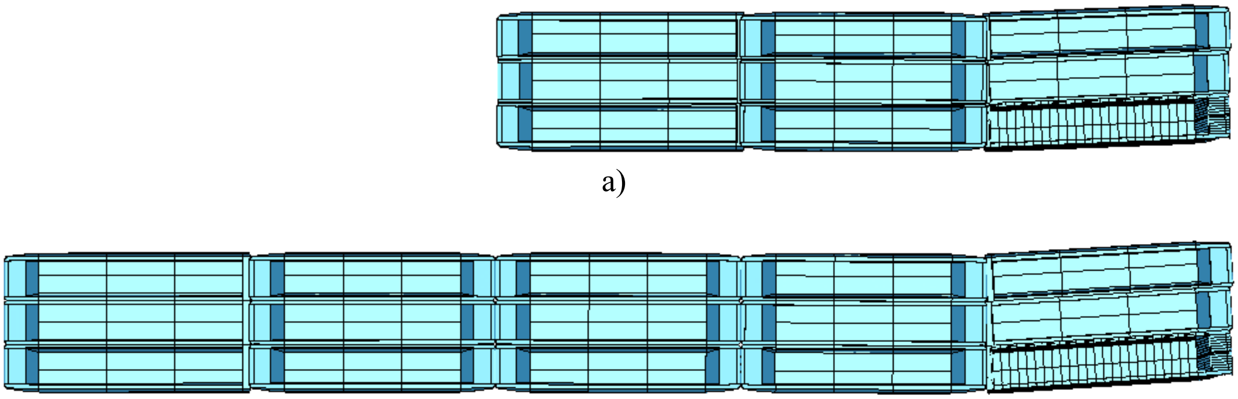

a)

b)

Figure 5.9. Barge flotilla deformation for impact condition 20° and 3 fps (displacements scaled by factor of 50 and flexible wall removed for clarity): a) 3x3 barge flotilla; b) 3x5 barge flotilla

This explanation is further corroborated by the force time-histories shown in Figures 5.10 to 5.14, which compare the 3x3 and 3x5 barge flotilla results for matching impact conditions. Evident in each plot is the fact that the force time-histories for the 3x3 and 3x5 flotillas are nearly identical through the first impact pulse, particularly for shallow angle impacts (10° and 20°). In the steeper angle (30°) impact cases, impact force time-histories agree not only through the first pulse, but also through the second pulse as well. In the 30° cases, multiple pulses of significant impact load occur, but forces generated during the first pulse are still reasonable approximations of overall maximum force arising during the entire collision event.

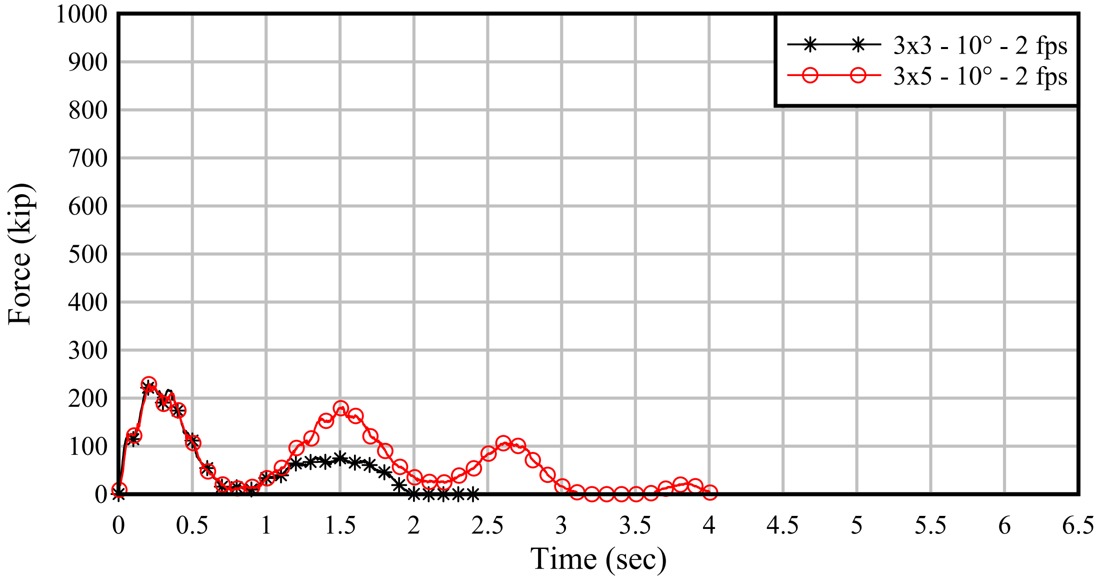

Figure 5.10. Force time-histories for 3x3 and 3x5 barge flotillas impacting at 10° with 2 fps initial velocity

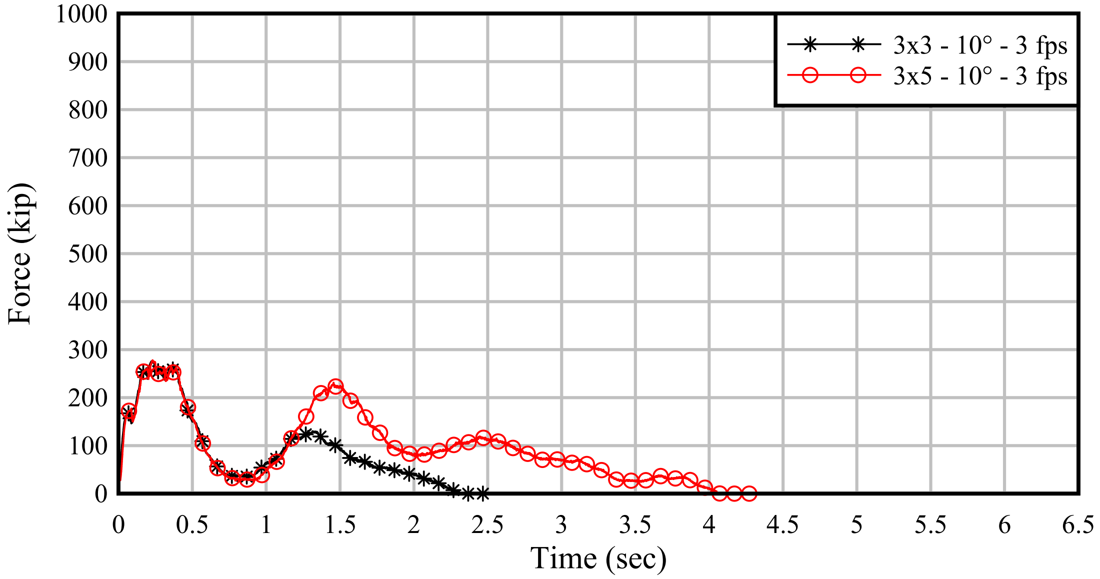

Figure 5.11. Force time-histories for 3x3 and 3x5 barge flotillas impacting at 10° with 3 fps initial velocity

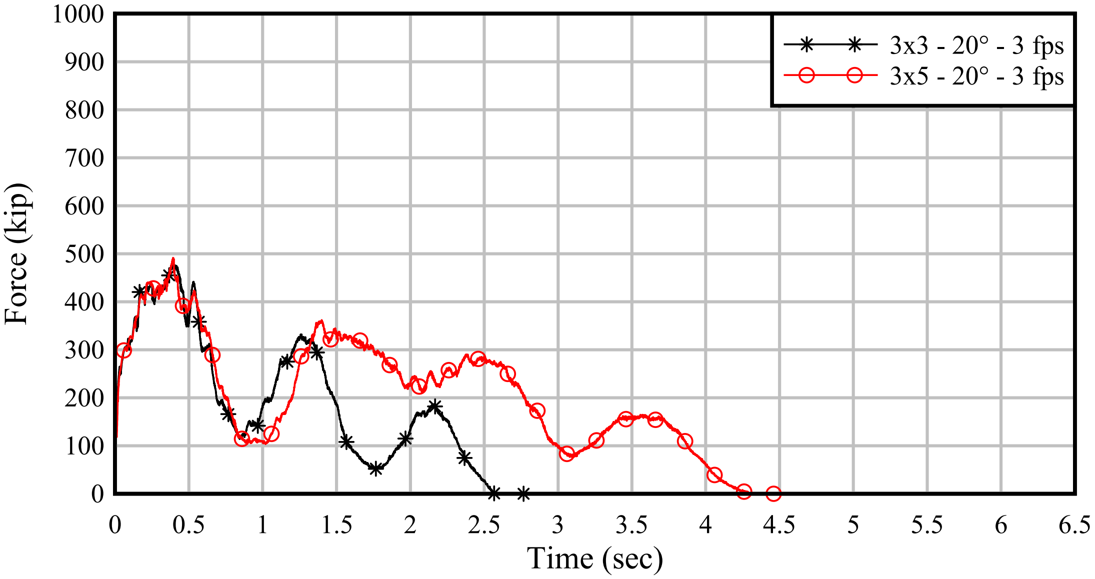

Figure 5.12. Force time-histories for 3x3 and 3x5 barge flotillas impacting at 20° with 3 fps initial velocity

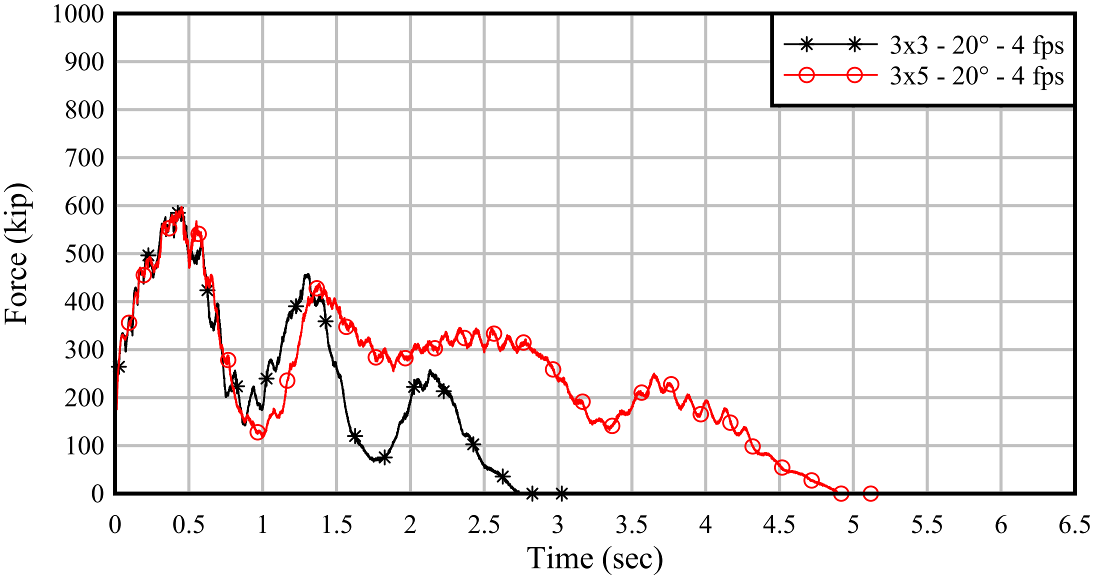

Figure 5.13. Force time-histories for 3x3 and 3x5 barge flotillas impacting at 20° with 4 fps initial velocity

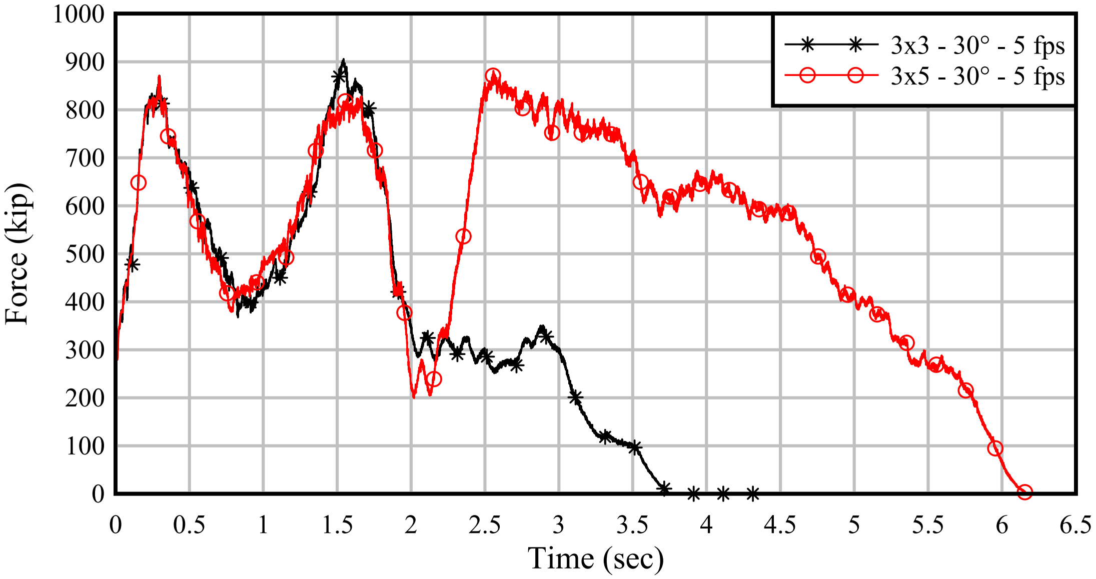

Figure 5.14. Force time-histories for 3x3 and 3x5 barge flotillas impacting at 30° with 5 fps initial velocity

The relationship revealed by this study between flotilla size, flotilla deformation, and impact force has important implications for the future development of an equivalent-static impact force prediction method (i.e., a new design standard). Previous design methodologies developed by the USACE, such as ETL (Engineer Technical Letter) 1110-2-563 (USACE 2004), have correlated impact force to total momentum (where both the force and momentum are measured in the direction normal to the impacted surface). However, the findings of this study suggest that flotilla momentum alone may not be an adequate predictor of impact force. Figure 5.15 presents results for all 3x3 and 3x5 barge flotilla impacts considered in this study by plotting peak impact force as a function of momentum (where both force and momentum are in the direction normal to the wall). In the figure, impact cases that generate the same impact force (due to having the same impact angle and speed, but differing momentums) are bounded by a dashed box. As evidenced by the figure, peak impact forces cannot be uniquely correlated to momentum. In particular, at high levels of impact momentum (i.e., severe, high-energy impacts), a wide range of differing momentums may result in the same peak impact force.

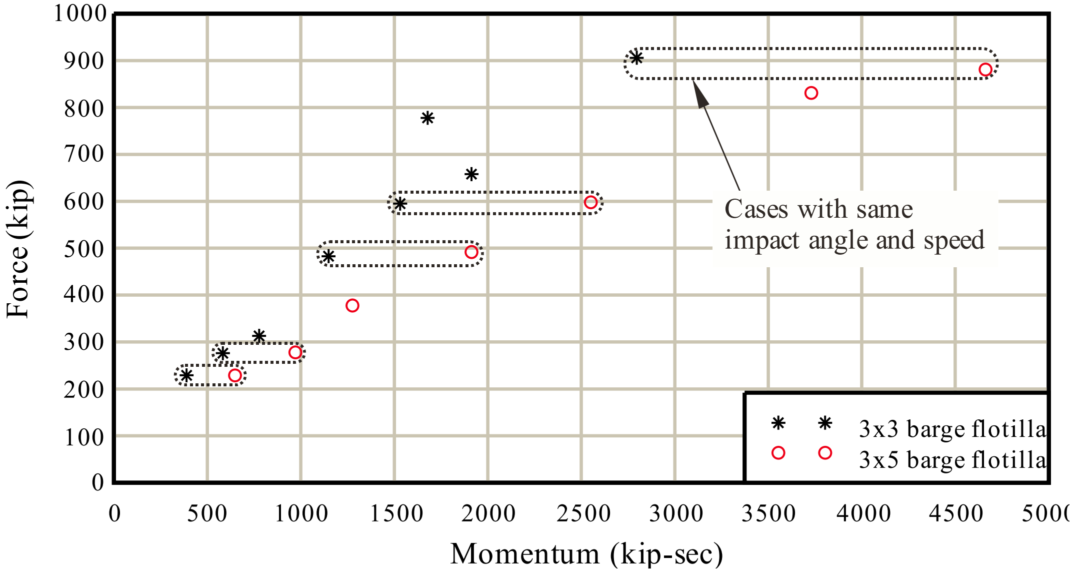

Figure 5.15. Peak impact forces plotted as a function of momentum
(both quantities correspond to the direction normal to the flexible wall)

5.3 Sensitivity of barge flotilla impact forces to flotilla size

Considering the findings presented above, it is desirable to determine the minimum barge flotilla length required to generate a peak impact force that is equivalent to that produced by the 3x3 and 3x5 barge flotillas. Hence, four additional impact simulations are conducted, each using a unique barge flotilla size (1x3, 2x3, 3x2, and 3x1) to further explore the relationship between flotilla size and peak impact force. Each of these additional flotilla impact simulations is conducted at an angle of 20° and at an impact speed of 3 fps. An illustration of each barge flotilla utilized (1x3, 2x3, 3x2, and 3x1) is provided in Figure 5.16. Note that each of these flotilla finite element models is created by deleting appropriate portions of the 3x3 barge flotilla model presented earlier.

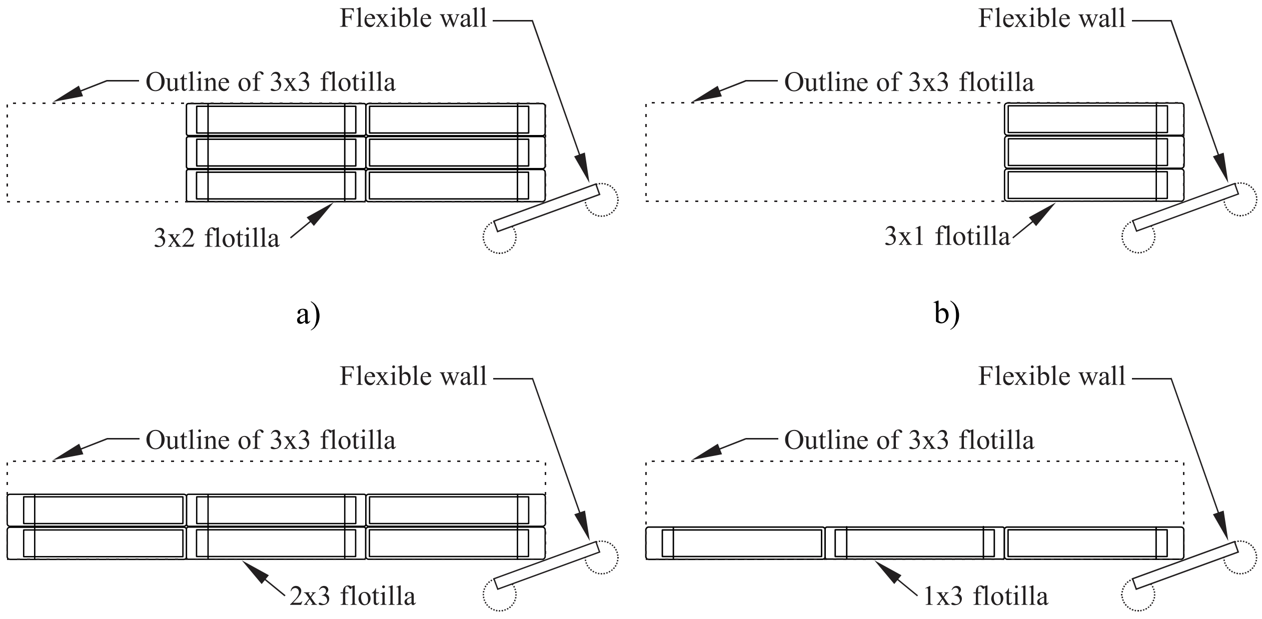

a) b)

c) d)

Figure 5.16. Barge flotilla configurations considered in sensitivity study:
a) 3x2 flotilla; b) 3x1 flotilla; c) 2x3 flotilla; d) 1x3 flotilla

Time-history force results from the four additional simulations are presented in Figures 5.17 and 5.18, which illustrate the effects of varying flotilla length and flotilla width, respectively. Impact forces presented are in the direction normal to the impact face of the flexible wall. Peak force results are also summarized in Tables 5.5 and 5.6. From Figure 5.17 and Table 5.5, it is evident that flotilla length has little influence on peak impact force generated. Even the single row (three wide) 3x1 flotilla is capable of producing a peak impact force that is within 10% of that produced by a 3x3 flotilla. This result further corroborates the notion that the magnitude of the initial pulse of impact force generated during a collision is primarily attributable to redirection of the first row of barges, regardless of the overall length of the flotilla.

Results presented in Figure 5.18 and Table 5.6, reveal that, unlike flotilla length, flotilla width has a significant influence on peak force generated during impact. Since changing the flotilla width involves changing the mass contained within the first row, it is logical that peak impact force will decrease as the width (and therefore mass) of the lead row decreases. An interesting consequence of this finding may be that since two flotillas of equal mass (and therefore equal cargo carrying capacity) but differing widths (e.g. a 3x2 and a 2x3) produce different impact forces for the same impact angle and speed, in selected circumstances, it might be possible to limit the impact forces generated on navigational structures by limiting the width of barge flotillas that operate on a particular section of waterway.

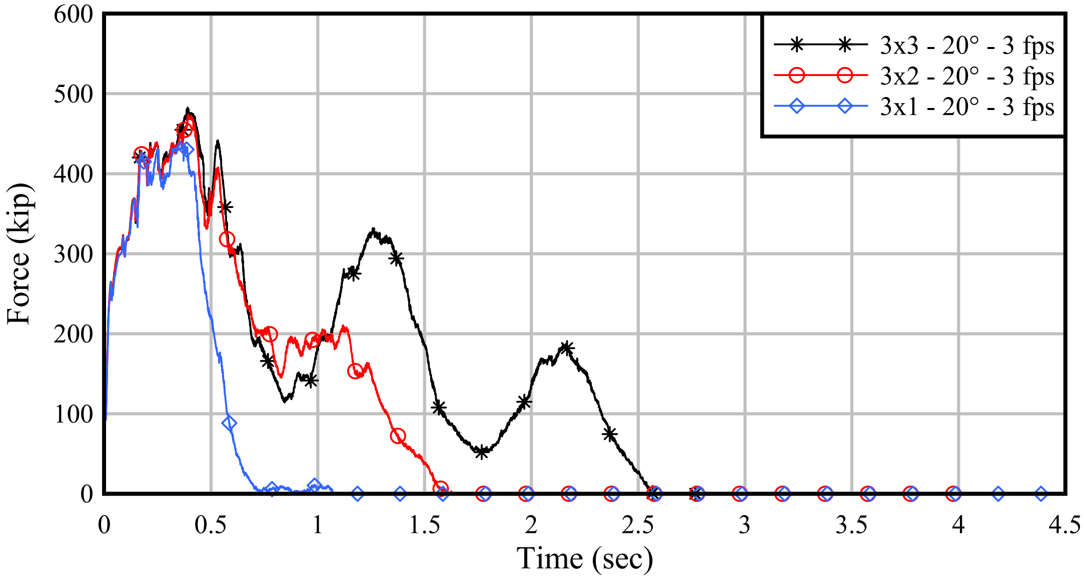

Figure 5.17. Effect of flotilla length on impact force time-histories

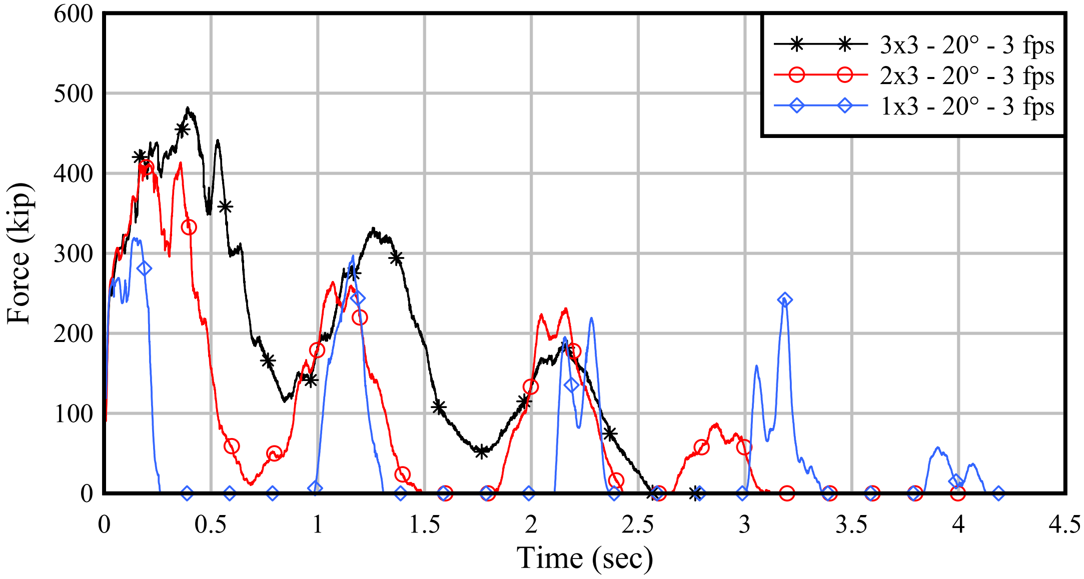

Figure 5.18. Effect of flotilla width on impact force time-histories

Table 5.5. Effect of flotilla length on peak impact forces

Flotilla configuration	Flotilla weight (kip)	Peak normal impact force (kip)	Total impulse of impact (kip-sec)
3x3	36000	483	540
3x2	24000 (-33%)	474 (-2%)	372 (-31%)
3x1	12000 (-67%)	440 (-9%)	195 (-64%)

Table 5.6. Effect of flotilla width on peak impact forces

Flotilla configuration	Flotilla weight (kip)	Peak normal impact force (kip)	Total impulse of impact (kip-sec)
3x3	36000	483	540
2x3	24000 (-33%)	414 (-14%)	359 (-34%)
1x3	12000 (-67%)	319 (-34%)	177 (-67%)

CHAPTER 6
CONCLUSIONS

In this study, a finite element model of a flexible guide wall currently in service at the Winfield Lock and Dam, WV, was developed, verified, validated, and subjected to simulated barge flotilla impacts for the purpose of quantifying impact forces. The finite element wall model accounts for the segmental post-tensioned nature of the physical wall at Winfield Lock and Dam, the variable cross-sectional shape of the wall, nonlinear concrete and mild reinforcing steel behavior, the effects of post-tensioning (including elastic shortening), and approximation of bearing pad stiffness, among other issues. Nonlinear static flexural response of the finite element wall model was verified against results obtained using an independent (and previously validated) sectional analysis calculation procedure.

The flexible wall finite element model was then combined with previously developed models of 3x3 and 3x5 barge flotillas to facilitate dynamic barge-wall impact simulations. Validation of the combined wall and barge flotilla models was carried out by conducting simulations of two full-scale impact experiments conducted by the US Army Corps of Engineers (USACE) at the Winfield Lock and Dam. Because the physical experiments conducted at Winfield utilized a relatively stiff steel load-measurement beam that was affixed to the impacting barge, a finite element model of this same load-measurement device was developed in this study and included in the validation impact simulations. Force time-histories from impact simulations were compared to data gathered during the Winfield impact experiments, and, for the two impact conditions examined, peak impact forces from the simulations were within approximately 10% of the peak forces measured during the experiments. Additionally, the stiffness of the load-measurement beam was found to alter the magnitude of forces generated during impact. A comparison of results from finite element impact simulations of barge flotillas with and without a load-measurement beam revealed that the presence of the load-measurement beam artificially increased the impact forces by approximately 20%.

Following validation, a set of fifteen (15) dynamic, nonlinear finite element impact simulations were conducted on the flexible wall model using both 3x3 and 3x5 barge flotilla models. Impacts were conducted at angles ranging from 10° to 30° and for impact velocities ranging from 2 ft/sec to 5 ft/sec. Unexpectedly, simulation results revealed that 3x3 and 3x5 barge flotillas produce nearly equal peak impact forces when impacting the flexible wall at the same angle of obliquity and impact velocity. To aid in understanding this phenomenon, four (4) additional impact simulations were conducted for reduced barge flotilla sizes of 3x2, 3x1, 2x3, and 1x3. By comparing data from impact simulations involving 3x5, 3x3, 3x2, 3x1, 2x3, and 1x3 barge flotillas, it was determined that peak impact forces are primarily a function of the mass contained within the first (fore-most) row of barges in the flotilla. Due to the relative flexibility of the lashings, during a flotilla-wall collision event, only barges in the fore-most row of the flotilla are redirected immediately by the wall. Because maximum impact forces generally occur during the first load pulse, when only the fore-most barge row is being redirected, peak impact forces correlate to the mass of the lead row, not the mass of the entire flotilla.

This finding has important implications for the future development of an updated equivalent-static load prediction method for use in the design of navigational guidance structures. The practice of relying on linear momentum as a predictor of impact force, as has been used in the development of past design methodologies, is not likely to lead to the most efficient and economical design standards if applied to multi-barge flotilla impact scenarios. A more refined approach in which flotilla momentum is supplemented with additional items of data, such as geometric configuration information, will be required if a simple and conservative, yet accurate (and therefore economical) impact load-prediction procedure is to be developed.

REFERENCES

ACI Committee 318 (2008), “Building Code Requirements for Structural Concrete (ACI 318-08),” American Concrete Institute, Farmington Hills, Michigan.

American Association of State Highway and Transportation Officials (AASHTO), *AASHTO LRFD Bridge Design Specifications,* 4th Edition, AASHTO, Washington D.C., 2007.

Barker, B.C., Ebeling, R.M., Gray, C.E., Haskins, R.W., and Warren, T.W. (In press). *Barge impact experiments at Winfield Lock and Dam,* Winfield, West Virginia. Vicksburg, Mississippi: U.S. Army Engineer Research and Development Center.

Collins, M. P., and Mitchell, D. (1991), *Prestressed Concrete Structures*, Prentice-Hall, Englewood Cliffs, New Jersey.

Consolazio, G.R., Fung, J., Ansley, M., “M-Φ-P Diagrams for Concrete Sections Under Biaxial Flexure and Axial Compression”, *American Concrete Institute (ACI) Structural Journal*, Vol. 101, No. 1, 2004, pp. 114-123.

Consolazio, G.R., Woolf, E., *Advanced Algorithms for Computing Moment-Curvature Relationships for Concrete Sections*. Structures Research Report No. 2007/65163, University of Florida, Gainesville, Florida, 2007.

Consolazio, G.R., Walters, R.A., Harper, Z.S., *Development of Finite Element Models for Studying Multi-barge Flotilla Impacts*. Structures Research Report No. 2010/87754, University of Florida, Gainesville, Florida, 2010.

Gent, A. N. (2001) *Engineering with Rubber: How to Design Rubber Components*, Hanser Gardner Publications, Cincinnati, Ohio.

Hsu, Thomas T.C. (1993), *Unified Theory of Reinforced Concrete,* CRC Press, Boca Raton, Florida.

Jones, N. (1997). *Structural Impact*, Cambridge University Press, Cambridge, U.K.

LSTC, *LS-DYNA Keyword User’s Manual: Version 971*, Livermore Software Technology Corporation, Livermore, California, 2009.

Nilson, A. H. (1987). *Design of Prestressed Concrete*, John Wiley & Sons, Hoboken, New Jersey.

Patev, R.C., Barker, B.C., Koestler III, L.V., *Full-Scale Barge Impact Experiments, Robert C. Byrd Lock and Dam, Gallipolis Ferry, West Virginia,* U.S. Army Corps of Engineers Research and Development Center, ERDC/ITL TR-03-7, Vicksburg, MS, 2003.

Tedesco, J.W., McDougal, W.G., Ross, C.A. (1999) *Structural dynamics: theory and applications*, Addison Wesley Longman, Inc., Menlo Park, California.

U.S. Army Corps of Engineers, *Barge Impact Analysis for Rigid Walls,* Engineer Technical Letter 1110-2-563, U.S. Army Corps of Engineers (USACE), Washington D.C., 2004.

U.S. Army Corps of Engineers, *2007 Flood Control and Navigation Maps: Mississippi River,* U.S. Army Corps of Engineers (USACE), Washington D.C., 2007.